Photonic circuits written by femtosecond laser in glass: improved fabrication and recent progress in photonic devices

Dezhi Tan[ORCID],[a,]* Zhuo Wang,[a] Beibei Xu,[a] and Jianrong Qiu[a,b,]*

[a]Zhejiang University, College of Optical Science and Engineering, State Key Laboratory of Modern Optical Instrumentation, Hangzhou, China
[b]Chinese Academy of Sciences, CAS Center for Excellence in Ultra-Intense Laser Science, Shanghai, China

Abstract. Integrated photonics is attracting considerable attention and has found many applications in both classical and quantum optics, fulfilling the requirements for the ever-growing complexity in modern optical experiments and big data communication. Femtosecond (fs) laser direct writing (FLDW) is an acknowledged technique for producing waveguides (WGs) in transparent glass that have been used to construct complex integrated photonic devices. FLDW possesses unique features, such as three-dimensional fabrication geometry, rapid prototyping, and single step fabrication, which are important for integrated communication devices and quantum photonic and astrophotonic technologies. To fully take advantage of FLDW, considerable efforts have been made to produce WGs over a large depth with low propagation loss, coupling loss, bend loss, and highly symmetrical mode field. We summarize the improved techniques as well as the mechanisms for writing high-performance WGs with controllable morphology of cross-section, highly symmetrical mode field, low loss, and high processing uniformity and efficiency, and discuss the recent progress of WGs in photonic integrated devices for communication, topological physics, quantum information processing, and astrophotonics. Prospective challenges and future research directions in this field are also pointed out.

Keywords: photonic integrated circuit; waveguides; femtosecond laser direct writing; improved techniques; photonic devices.

1 Introduction

Photonic integrated circuits have shown the potential to allow integrating passive and active optical components on one chip in a scalable manner and have been identified to support a plethora of applications, such as data communication, sensing, astrophotonics, quantum information processing, and national security.[1–4] Photonic circuits are indispensable components in modern optical communication networks and lie at the heart of integrated photonic devices. Currently, to this end, one of the biggest challenges in integrated photonics is establishing a general and flexible method to produce photonic circuits with low loss, high integration density, and high tunability. The unique feature of 3D fabrication geometry promises

femtosecond laser direct writing (FLDW) as an on-demand solution to these requirements.

Femtosecond (fs) laser-induced multiphoton absorption enables tailoring the material structures and properties inside transparent bulk materials with high processing precision and triggers a great deal of activity in the field of photonics.[5–13] In particular, the fs laser can induce a permanent refractive index change in glass, which indicates a promising tool to fabricate photonic circuits, waveguides (WGs), and basic elements in integrated optics.[5,14,15] FLDW has been identified to be an effective technique for constructing WGs in a 3D fashion over a large depth from the micrometer to millimeter scale.[5,16–18] WG-based 2D and 3D optical devices have also been demonstrated in various glasses. Compared with the 2D fabrication of silicon photonic circuits by planar lithography, FLDW is a rapid prototyping technique to produce WGs in 3D without needing complex procedures. Thus, up to now, FLDW has been exploited to

*Address all correspondence to Dezhi Tan, wctdz@zju.edu.cn; Jianrong Qiu, qjr@zju.edu.cn

be a highly potential solution to quickly create optical components and integrated photonic devices three-dimensionally in transparent glasses. The intrinsic characteristic of being embedded in bulk makes these devices highly tolerant to variations of the working environment, which is significant for optical network applications.[19,20]

However, although significant advances have been made in writing and applications of WGs, there are still practical challenges that need to be addressed before fully exploiting 3D fabrication capabilities of FLDW and constructing complex WG-based photonic integrated devices. For example, low insertion loss, including low coupling loss and propagation loss, and symmetrical mode field are usually necessary. Unfortunately, propagation effects, such as nonlinear filamentation and refocusing, would influence energy-deposition behavior and the resultant microstructures.[21,22] In general, when a tightly focused fs laser irradiates into glass, a refractive-index mismatch between the air and glass causes spherical aberration (SA), which would distort the energy distribution in the focus and the shape of modified volumes.[23–25] SA increases with increments of numerical aperture (NA), focusing depth, and refractive index of the glass.[26] Other effects such as the self-focusing effect and nonlinear absorption effect can also induce focus distortion. As a result, although the transverse writing geometry with the writing direction perpendicular to the laser propagation axis can realize maximum degrees of processing flexibility, these effects intrinsically lead to an elliptical cross-section in WGs and usually also cause high asymmetry in the mode field of the written WGs along with high coupling loss and propagation loss.[15,27,28] It is a great challenge to maintain the WG circularity, symmetry, and mode-field profiles, which would limit the coupling loss, propagation loss, and 3D capability of the FLDW technique. Furthermore, these issues will be more serious for the deep WGs in glass. However, writing deep WGs is of importance for constructing complex reconfigurable photonic circuits, which is essential for highly integrated on-chip devices with multifunctionality. Furthermore, to push the development and wide-scale implementation of integrated photonic devices beyond the laboratory, the importance of fabricating WGs with high uniformity and efficiency is continuing to grow, which raises concerns over controlling the highly nonlinear process in the WG writing and the stability of the setups. In addition, since the refractive index change induced by fs laser irradiation is generally small (usually smaller than 1%), decreasing the loss, especially the bend loss in the curved WGs, is a tough task. To address these issues, great efforts have been devoted to developing improved strategies to reduce the coupling loss, propagation loss, and bend loss, improve the symmetry of cross-section and that of the mode field, and enhance the processing uniformity and efficiency.

Here, we provide a comprehensive review of the improved techniques along with the mechanisms for controlling the symmetry of the WG cross-section and mode field profile and reducing the loss (including coupling loss, propagation loss, and bend loss), as outlined in Fig. 1. Furthermore, with the ever-increasing data demand, photonic WGs have achieved explosive growth in applications, especially in optical communication devices, topology and quantum science, and astrophotonics. We will also review the state-of-the-art progress of photonic applications in these fields with WGs written by fs lasers.
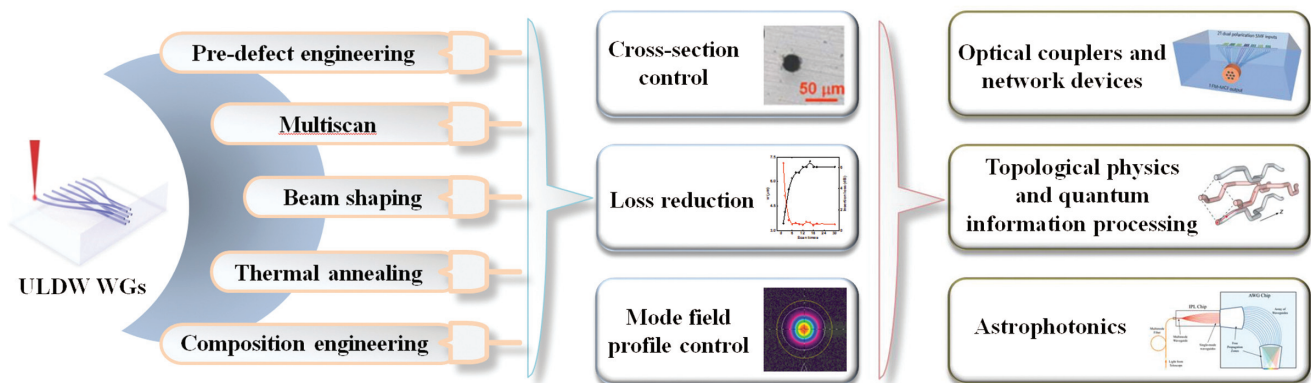
2 Improved Technologies and Mechanisms for Waveguide Writing by Femtosecond Lasers

2.1 Beam Shaping

The shape of the focal volume affects the energy distribution and the generated cross-section of the WGs, which would determine the morphology of the mode field, the coupling loss, and propagation loss.[15,28] In general, manipulating the beam shape has been proved to be a facile method to control the morphology of the mode field and reduce the coupling loss and propagation loss. For this purpose, several beam shaping techniques were introduced, including slit beam shaping, astigmatic beam shaping, simultaneous spatiotemporal focusing (SSTF), and spatial light modulator (SLM) beam shaping.[23–26,29–32]

2.1.1 Slit beam shaping

In general, as mentioned, WGs written by fs lasers in glass using conventional spherical focusing optics exhibit significant loss and strong core asymmetry with an elongated shape along the fs laser propagation direction with a large aspect ratio. Cheng et al. reported that the aspect ratio in the cross-section of the microchannels could be greatly reduced by inserting a

Fig. 1 WGs written by fs lasers in glass: improved fabrication techniques and photonic device applications.

slit before the focusing lens with the slit oriented parallel to the laser scanning direction, which is attributed to the diffraction effect at the slit aperture.[23] This slit beam shaping technique was also adopted to produce low loss, circular WGs in glass with a long working-distance objective lens.[25,33,34]

For a circular Gaussian beam and an elliptical Gaussian beam, the energy distribution near the focal point is described as[23]

$$I_c = \frac{1}{(1 + z^2/z_0^2)} \exp\left[-2\frac{x^2 + y^2}{w_0^2(1 + z^2/z_0^2)}\right], \tag{1}$$

$$I_e = \frac{1}{(1 + z^2/z_0^2)^{1/2}} \frac{1}{(1 + z^2/z_0'^2)^{1/2}} \exp\left[-2\frac{x^2}{w_0^2(1 + z^2/z_0^2)}\right]$$
$$\times \exp\left[-2\frac{y^2}{w_0'^2(1 + z^2/z_0'^2)}\right], \tag{2}$$

where $w_0 = \lambda/(\text{NA} \cdot \pi)$ is the beam waist at the focus with λ as the laser wavelength, $z_0 = kw_0^2/2$ is the Rayleigh length with k as the wave vector, and $w_0' = (R_x/R_y)w_0^2$ and $z_0' = kw_0'^2/2$ with R_x and R_y as the radii along the x and y axes of the elliptical beam, respectively. Equation (2) indicates that a beam waist can be expanded R_x/R_y times in the y direction, and the beam in the x direction is tightly focused, leading to small Rayleigh length. As a result, for an elliptical Gaussian beam, there is a significant reduction in the aspect ratio that is determined by the ratio of the Rayleigh length to the beam waist at the focal point, which is achievable by inserting a slit.[23,26]

To estimate the optimal slit width (W_y) for generating highly symmetrical cross-section of WGs, the aspect ratio of the slit, W_y/W_x, can be expressed as the following:

$$\frac{W_y}{W_x} = \frac{\text{NA}}{n} \sqrt{\frac{\ln 2}{3}} \quad \text{for } W_x > 3W_y, \tag{3}$$

where W_x is the unapertured beam waist, NA is the numerical aperture of the objective lens, and n is the refractive index of glass.

Compared to the case without a slit, as shown in Fig. 2(a), Fig. 2(d) shows that the transverse width in the y direction has become significantly larger by placing a slit before the focusing lens, which results in much higher symmetry for the energy distribution [Fig. 2(e)]. Figure 2(c) shows that the shape of a WG written without a slit has an elliptical-shaped core with the aspect ratio of about 4:1. A circular WG is fabricated by introducing a slit with width of about 500 μm, as shown in Fig. 2(f). The symmetry of the refractive index distribution and mode field of the guiding light also becomes higher after inserting a slit. Consequently, this slit beam shaping would be favorable for improving the loss performance.

Combining low NA ($0.1 - 0.2$) focusing optics and the slit beam shaping technique, the fs laser could write deep surface WGs with a circular cross-section and low loss over a large depth range (e.g., from 0.7 to 7 mm), and the aspect ratio reaches nearly 1.[26] Due to the highly symmetrical morphology, Fig. 2(h) shows that the propagation loss is as low as 0.2 dB/cm at the depth of 0.72 mm and remains smaller than 1 dB/cm at the depth beyond 7 mm. The slit beam shaping technique also works in the transverse regime with the laser beam moving

along the propagation direction.[35] All of these results reveal that slit beam shaping is a powerful technique to improve the performance of WGs written by fs lasers in glass. In addition, the slit beam shaping technique is also adopted to fabricate WG Bragg gratings with a circular cross-section.[36,37]
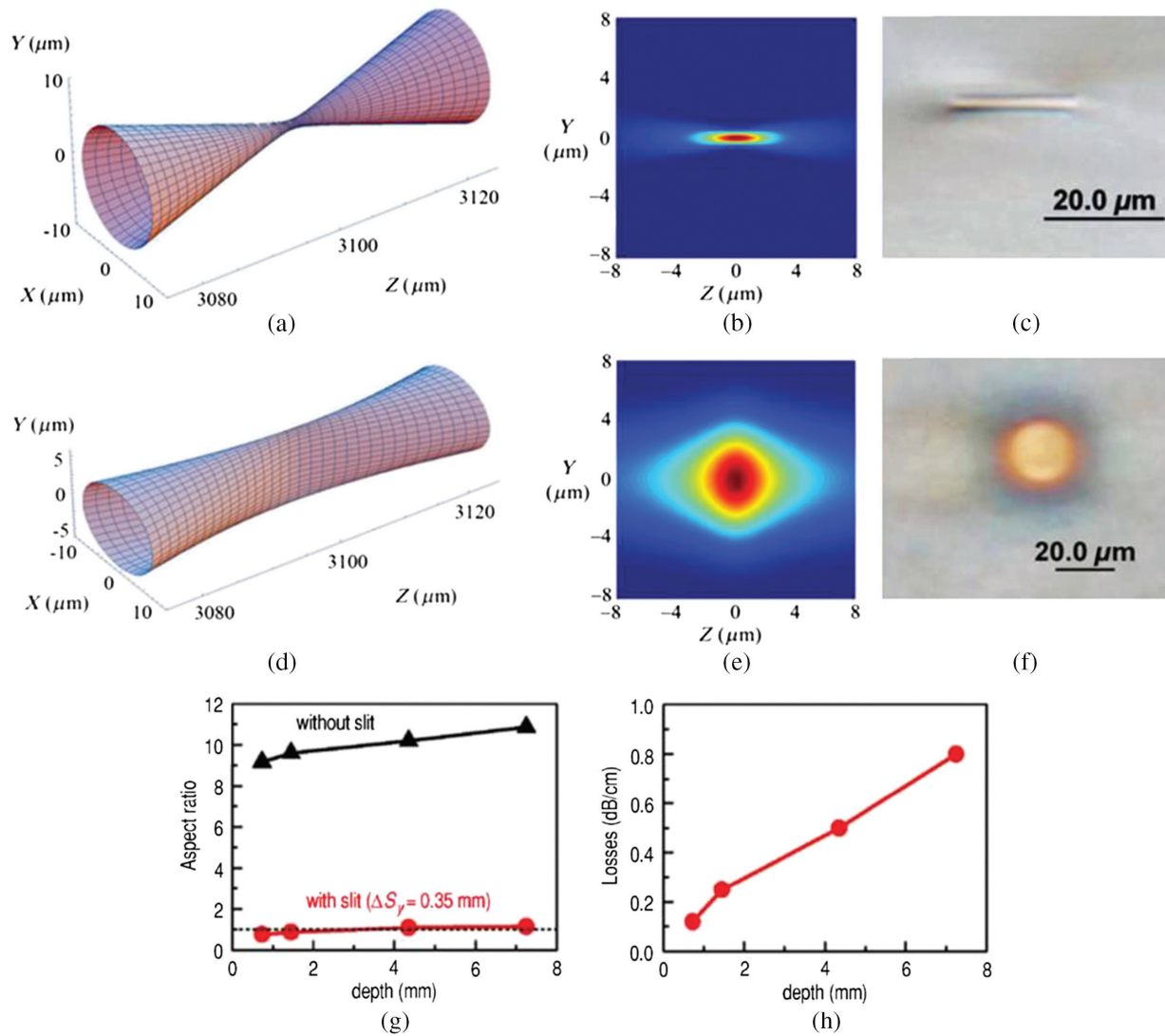
2.1.2 Astigmatic beam shaping

Although the slit beam shaping technique is simple, it is not efficient, and most of the laser energy is attenuated by the slit.[32,38] To shape the laser beam, astigmatic shaping is also adopted to reshape the beam with an astigmatic cylindrical telescope before focusing, which allows for writing WGs with a circular cross-section and arbitrary size.[29,31,39–44] The basic principle for the astigmatic beam shaping is that the WG size does not depend on the focal size along the sample translation direction in the transverse writing regime. Focusing very tightly in the x direction will decrease the Rayleigh range z_{Rx}; the increased divergence in the xz plane can significantly reduce the intensity to that below the threshold for nonlinear absorption, and this decreases the focus depth. Consequently, the transverse WG size can be optimized by independently tuning the focal size in the y direction. The intensity profile of a focused astigmatic Gaussian beam can be expressed as

$$I_0(x, y, x) = I_{00} \frac{w_{ox}}{w_x(z)} \frac{w_{oy}}{w_y(z)} \exp\left\{-2\left[\frac{x^2}{w_x(z)^2} + \frac{x^2}{w_y(z)^2}\right]\right\}, \tag{4}$$

$$w_x(z) = w_{ox}\sqrt{1 + \left(\frac{z}{z_{Rx}}\right)^2}, \quad w_y(z) = w_{oy}\sqrt{1 + \left(\frac{z - z_0}{z_{Ry}}\right)^2}, \tag{5}$$

where $z_{Rx,y} = \pi(w_{0x,y}^2/\lambda)$ denotes the Rayleigh ranges of the Gaussian beam for the x and y directions, w_{ox} is the astigmatic beam waist at $z = 0$, and z_0 is the offset distance between the beam waists, named the astigmatic difference, which is shown in Fig. 3(a). Increasing the beam size (w_y) in the y direction, with respect to w_{0y}, is achieved by controlling z_0 at the plane with respect to the beam waist in the x direction. Figures 3(a)–3(d) show that the symmetry and size of the electron density profile are highly tunable by modifying the astigmatic difference. Consequently, the WG size perpendicular to the beam propagation direction can be adjusted continuously, and the highly symmetrical WG profile is achievable. Furthermore, manipulating the astigmatic difference allows for not only improving the symmetry of the WG profile but also for varying the WG size. As a result, the coupling loss can reach as low as 0.1 dB/facet to the single mode optical fiber at 1550 nm, and the propagation loss is lower than 0.4 dB/cm.[45] This beam shaping method is also of significance for mass production of identical WGs, which provide a stable and reliable quantum light source.[39,40]

When the microstructure is not purely one-dimensional (1D), slit beam shaping and astigmatic beam shaping require modifying the orientation of the slit or the cylindrical lens pair during laser beam scanning, and an additional complexity is produced. As a result, they are not suitable for writing bending WGs and related devices that restrict their further applications.

Fig. 2 Beam evolution near focus (a) without and (d) with a slit, energy distribution in the YZ plane (b) without and (e) with a slit, optical images of fabricated WGs in phosphate glass (c) without and (d) with a slit ($W_y = 500\ \mu$m). X corresponds to the fs laser beam translation direction. Figures reproduced from Ref. 25. (g) Aspect ratio of the WGs produced in the fused silica with a slit W_y of 350 μm. Dotted line: aspect ratio of 1. (h) Propagation loss at 1550 nm as a function of depth ($W_y = 250\ \mu$m). Figures reproduced from Ref. 26.

2.1.3 Simultaneous spatiotemporal focusing

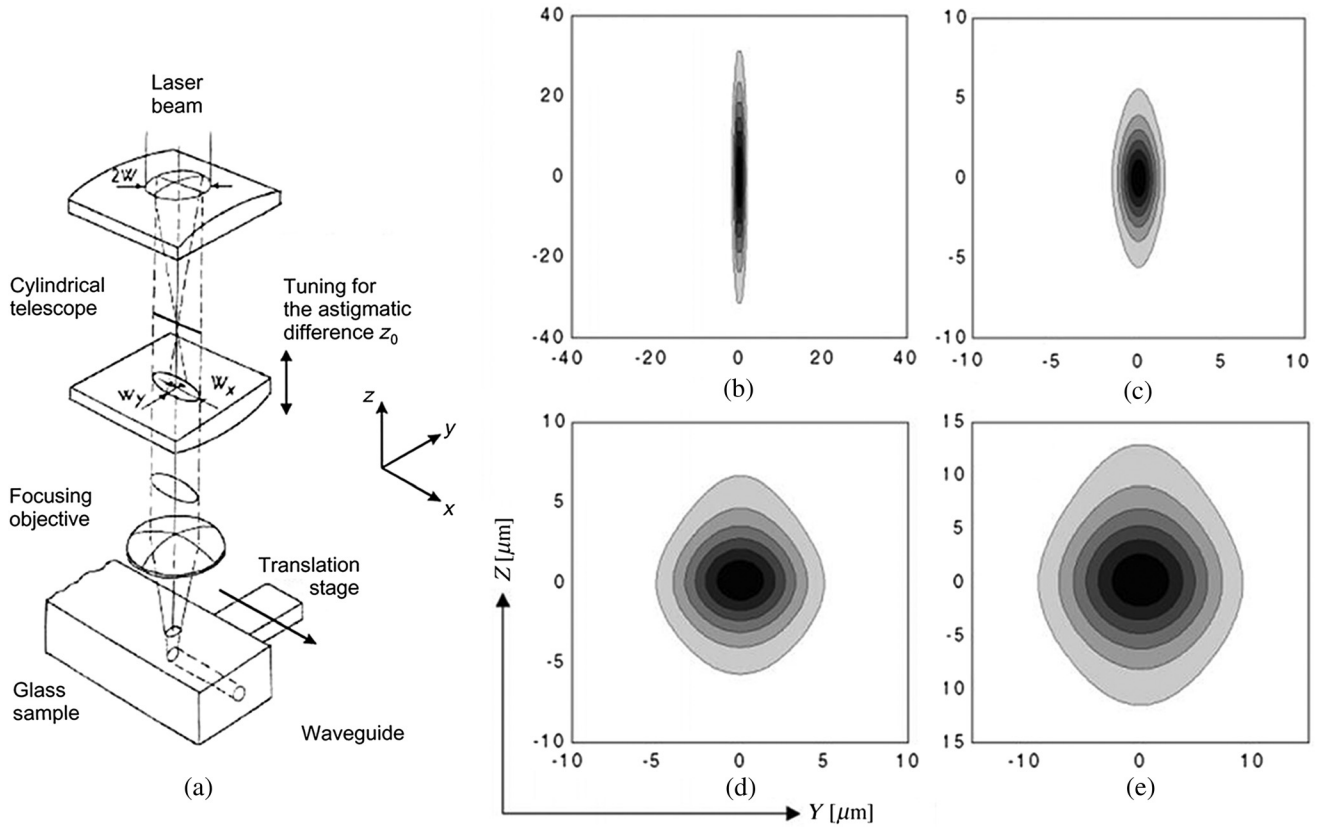SSTF offers another solution to control the cross-section.[30,46–49] This technique relies on separating the spectral components of the fs laser pulse in space before focusing using a grating pair, which induces spatial chirping in the incident pulse and generates an array of beamlets at various frequencies. As different frequency components overlap spatially only around the focus, temporal focusing happens, and this results in the shortest pulse duration with the highest peak intensity. In such a manner, the spatiotemporally focused pulses are transform-limited in time, diffraction-limited in space, and strongly localized near the geometric focus, and the pulse duration broadens obviously when moving away from the focus, which leads to a rapid decrease in the peak intensity. As a result, this transform-limited SSTF method allows for a significant improvement in the axial

resolution of the fs laser writing. The schematic illustration of fs laser SSTF is shown in Fig. 4(a).

In general, the field of a spatially chirped pulse can be written as

$$A_1(x, y, \omega) = A_0 \exp\left[-\frac{(\omega - \omega_0)^2}{\Omega^2}\right] \exp\left\{-\frac{[x - \Delta x(\omega)]^2 + y^2}{2W_0^2}\right\},$$

$$(6)$$

where A_0 is a field amplitude, $\sqrt{2 \ln 2}\Omega$ is the full width at half maximum of the frequency spectrum, ω_0 is the carrier frequency, W_0 is the incident beam waist before the grating pair, and $\Delta x(\omega) = \alpha(\omega - \omega_0)$ is the displacement of each spectral component (α is the groove density of the grating).

Fig. 3 (a) Schematic of the WG writing setup with astigmatic beam shaping. Figure reproduced from Ref. 31. Simulated electron density profiles (b) without and with astigmatic beam shaping for different focusing parameters (c) $w_{0x} = 1$ μm, $w_{0y} = 3$ μm, $z_0 = 0$, (d) $w_{0x} = 1$ μm, $w_{0y} = 3$ μm, $z_0 = 100$ μm, and (e) $w_{0x} = 1.4$ μm, $w_{0y} = 4.2$ μm, $z_0 = 260$ μm. Figures reproduced from Ref. 29.

The field after the objective lens and near the focus can be expressed as

$$A_2(x, y, \omega) = A_1(x, y, \omega) \exp\left(-ik\frac{x^2 + y^2}{2f}\right), \qquad (7)$$

$$A_3(x, y, \omega) = \frac{\exp(ikz)}{i\lambda z} \iint_{-\infty}^{\infty} A_2(\xi, \eta, \omega)$$
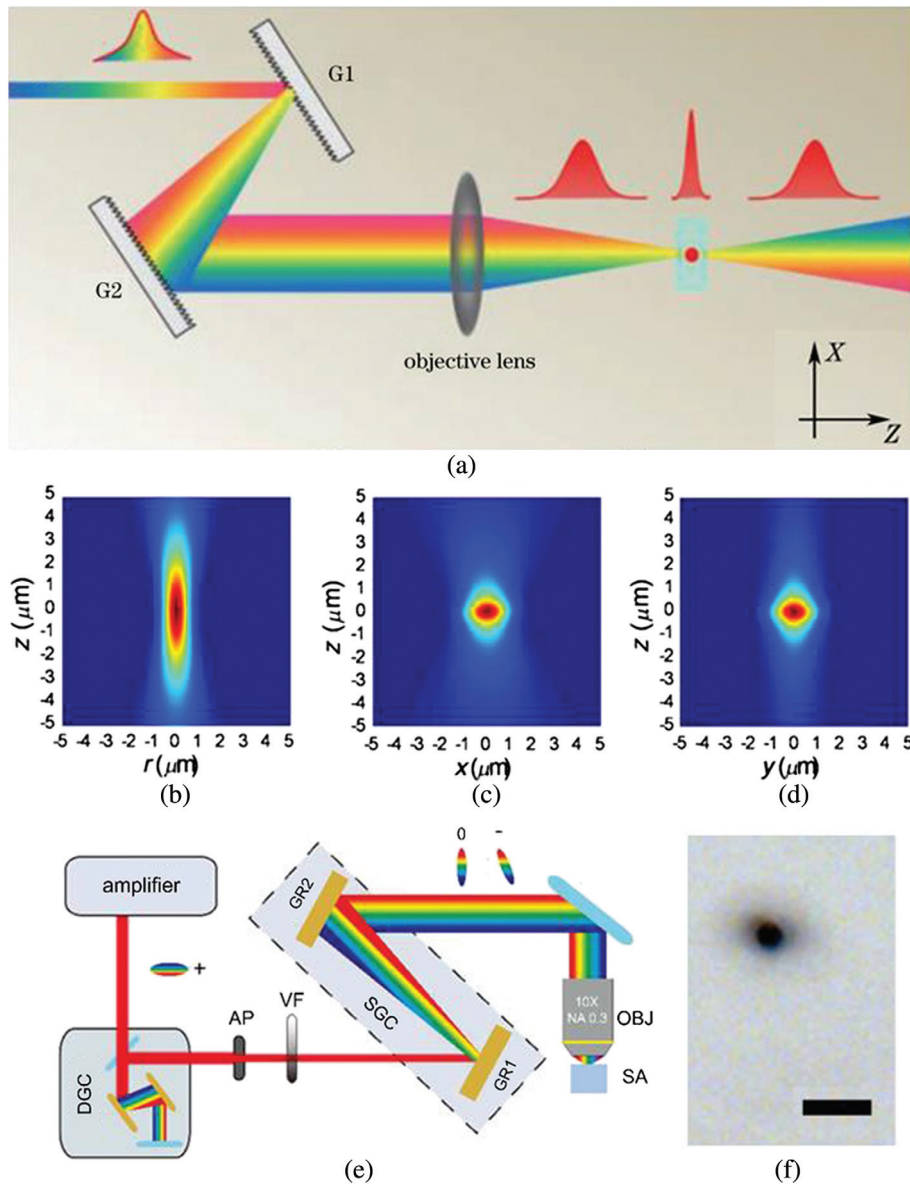$$\times \exp\left[ik\frac{(x - \xi)^2 + (y - \eta)^2}{2z}\right] d\xi\, d\eta, \qquad (8)$$

where k is equal to $2\pi c/\omega_0$, c is the velocity of light in vacuum, and f is the focal length of the objective lens.

$$I(x, y, z, t) = |A_3(x, y, z, t)|^2$$
$$= \left| \int_{-\infty}^{\infty} A_3(x, y, z, t) \exp(-i\omega t) d\omega \right|^2. \qquad (9)$$

Figures 4(c) and 4(d) show the intensity distributions of the SSTF beam in the XZ and YZ planes calculated by combining Eqs. (6)–(9), and a nearly spherical intensity distribution has been obtained. Furthermore, the axial resolution of fs laser writing is continuously tunable simply either by adjusting the incident beam size or the spatial chirp of the laser pulse via changing the distance between the two gratings. In addition, an objective lens with a relatively high NA (i.e., NA = 0.46) is necessary for generating a nearly spherical distribution of the laser field in the focal volume. However, a low NA objective lens cannot result in a circular lateral cross section.[50]

The aspect ratios of cross-sectional shapes of a focal spot can be manipulated independently in both axial and lateral directions by combining a slit beam shaping technique and an SSTF technique, which enables isotropic resolution in 3D space even for an objective lens with low NA.[51] To suppress the strong aberration in the fabrication at large depth, another double-pass grating compressor (DGC) can be adopted, as shown in Fig. 4(e). The total group delay dispersion of the pulse before the objective lens could be controlled by simultaneously modifying the DGC and the single-pass grating compressor. The longitudinal resolution is improved dramatically, and a nearly perfect circular cross-section is obtained. In this case, a low NA lens also works. The focal lens with low NA allows for writing circular WGs at a large depth (~9 mm), owing to its long working distance.[50] In addition, besides controlling the aspect ratio, SSTF also offers several additional levels of control over the ultrafast laser focus such as an adjustable pulse front tilt (PFT).[52,53] Neighboring foci can be overlapped by exploiting the inherent PFT with an appropriately designed diffractive holographic pattern from SLM irradiated

Fig. 4 (a) Schematic illustration of fs laser SSTF. Calculated laser intensity distributions at the focus generated by an objective lens (b) without and (c), (d) with the SSTF technique in the *XZ* and *YZ* planes, respectively. Figures reproduced from Ref. 30. (e) Schematic of the experimental setup for adding an initial temporal chirp on the SSTF. AP, aperture; VF, variable neutral density filter; GR1 and GR2, gratings; OBJ, objective lens; SA, sample. (f) Cross-sectional view optical micrographs of the line written at 9 mm. Scale bar, 20 μm. Figures reproduced from Ref. 50.

by a spatially chirped beam, and overlapping of multiple spots from a single pulse could have occurred in space but separated in time.[47] This technique not only provides a high level of axial confinement but also enables parallel writing for improving the processing efficiency. Temporally chirped SSTF is demonstrated via focusing the light with an off-axis parabola after the grating pairs, which is useful for rapid prototyping to produce high aspect ratio channels in glass and also for biomedical applications (e.g., deep tissue ablation and optical histology).[54] Combining a grating with an SLM or a cylindrical lens, temporally chirped SSTF is also achievable with enhanced axial resolution for accurately tailoring the laser–material interaction.[49,55,56]

In summary, the SSTF of the fs laser pulse strongly reduces nonlinear side effects and offers unique possibilities for fabrication with isotropic 3D resolution.[57] Furthermore, the addition of an initial temporal chirp on the SSTF is favorable for keeping the fabrication resolution nearly unchanged against the SA.

2.1.4 Spatial light modulator beam shaping

An SLM beam shaping technique gives rise to a versatile and energy efficient option for modifying the energy distribution in the focus, allowing not only for the improvement of the aspect-ratio of the focal volume as well as the symmetry of the mode field pattern of WGs but also the dynamic manipulation of it
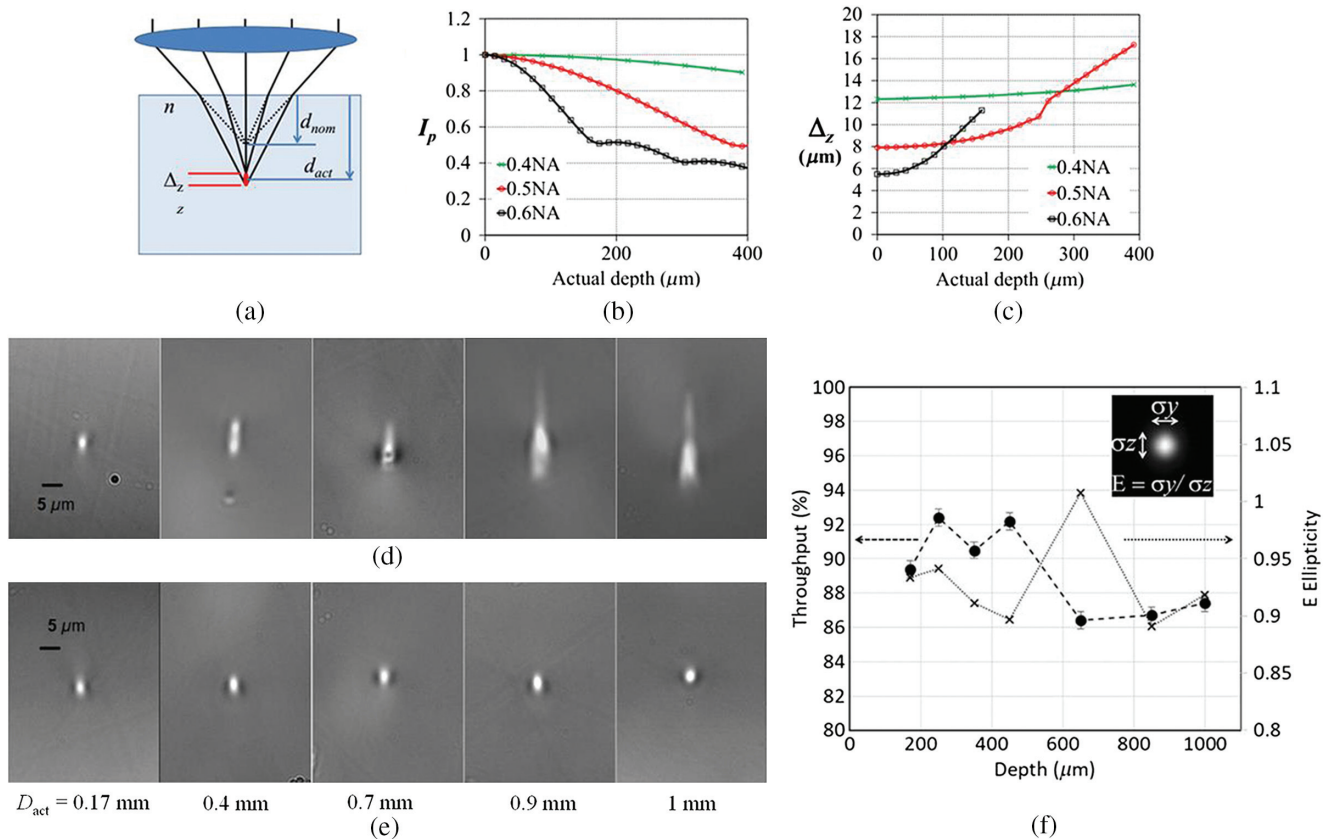
during fabrication.[24,58–60] Aberration correction is achieved over a large depth using SLM with higher accuracy and flexibility, which enables writing deep WGs with a circular cross-section. To realize the depth-dependent aberration correction, the change in optical path length for the light refracted at the glass surface should be considered, and the SA associated phase in the pupil of the objective can be expressed as[59]

$$\emptyset_{SA}(\rho) = \frac{-2\pi d_{\mathrm{nom}}}{\lambda}\left[\sqrt{n_2^2 - (\mathrm{NA}\cdot\rho)^2} - \sqrt{n_1^2 - (\mathrm{NA}\cdot\rho)^2}\right],$$
(10)

where d_{nom} is the nominal depth in the glass [Fig. 5(a)], λ is the wavelength of the fs laser, n_1 (n_2) is the refractive index of air (glass), ρ is the normalized pupil radius, and NA is the NA of the lens. Equation (10) indicates that the aberration strongly depends on writing depth and the NA of the objective lens. Figure 5(b) shows that the peak intensity (I_p) of the laser beam decreases with increase of focusing depth, especially in the higher NA regime. The full width at half maximum (Δz) of the distribution along the beam propagation direction increases with the depth, as revealed in Fig. 5(c), and this is in agreement with the simulation of energy distribution for focusing at various depths, which shows that the focus becomes distorted, and the cross-section is no longer symmetric and substantially elongated along the laser propagation direction. The distortion and asymmetry become more serious with a depth increase. As a consequence, the cross-section of the fabricated WGs is noncircular at the large depth, as shown in Fig. 5(d). Figure 5(e) shows that the morphology of the WG can be improved significantly after appropriate aberration correction using SLM, and the WG cross-section almost does not depend on the writing depth. Furthermore, Fig. 5(f) shows that the near-field mode profile exhibits high symmetry, and the mode ellipticity reaches nearly 1. In addition, there is also no obvious difference in light transmission of the WGs at different depths after aberration correction. These results indicate that the SLM beam shaping technique allows for fabricating symmetrical WGs through the entire depth of the working objective lens, which will be crucial for fabricating complex WG lattices with high integration density and holds promise for a wide range of applications with 3D photonic circuits.

In addition, the SLM can also enable effective parallel writing. Multiple foci with controlled power distribution and dynamically variable distance can be produced in 3D by modulating the spatial phase distribution of a fs laser beam with a computer-generated hologram, which allows for writing several WGs or multiscan performance over one WG in a single pass.[61–64] Furthermore, for fabricating 3D WG arrays and coupling devices

Fig. 5 (a) Schematic of the focusing geometry. (b) Simulated estimate of the focal peak intensity I_p at various depths in glass. (c) Δz as a function of depth. WGs inscribed at different depths (d) without and (e) with aberration correction in the nonthermal writing regime (pulse repetition rate of 1 kHz). Figures reproduced from Ref. 59. (f) Plot of the transmission throughput and mode ellipticity as a function of depth for WGs inscribed with SLM beam shaping at the thermal writing regime (pulse repetition rate of 1 MHz). Figure reproduced from Ref. 24.

using the traditional fs laser writing technique, the substrate is needed to be precisely positioned. With the help of the SLM, a branched WG can be written simultaneously by one pass scanning in glass. Consequently, an SLM not only significantly enhances the fabrication uniformity and efficiency but also eliminates the need for precisely positioning the glass substrate.

2.2 Multiscan

Multiscan is a reliable technique to increase the refractive index change and modify the shape and size of the WGs by scanning the laser beam multiple times.[5,65] In this regime, there is no position shift between consecutive scans. David et al. revealed that the increase in refractive index is about 0.01 and 0.035 in the Ge-doped silica glass generated by 1 and 10 writing passes, which indicates the possibility of reducing insertion loss by the multiscan.[5,65] Bend loss could be also reduced by scanning the WG track multiple times in all curved segments due to the tighter confinement of the modes caused by multiscan-induced large refractive index contrast.[66] Recently, Tan et al. reported that the WG size can be controlled by adjusting the scanning passes [Figs. 6(a)–6(c)].[67] Furthermore, a mechanism of a temperature gradient-assisted process was proposed for the formation of WGs, which locates outside the focus. Consequently, the unique position of WGs allows for abating the distortion of laser energy in the focal volume and inscribing low-loss deep WGs. Usually, a WG core with the largest density and RI locates near the center of the modified zone, which is generated by the matter melting and quenching in thermal writing with high repetition rate pulses (e.g., >100 kHz) or local compression in the nonthermal case with low repetition rate pulses. In temperature gradient-assisted writing, a high temperature with a sharp gradient is generated by ultrafast injection of enough energy in the focus, which is accompanied by pressure wave propagation. As a result, rapid mechanical expansion with structural reorganization is driven during the temperature evolution, and melted and ionized matter would be ejected out from the hot pressurized center to the surrounding zone, resulting in forming a densified "cladding" ring and a rarefied center consisting of less dense structures [Fig. 6(a)]. In addition, in the conical WG structure, a quasidirectional hydrodynamic material flow can be induced by the fast stress relaxation along the laser propagation axis, and the axial densification at the top of the densified ring is generated [Fig. 6(b)]. Multiscan writing is suggested to repeat this material flow process and increase the WG size. The absence of separation between the parallel pass avoids the presence of a nonhomogeneous interface structure between parallel scans. As the guiding core of WGs is at the tips of the densified zone, outside the focal volume, a lowest insertion loss of about 0.6 dB [Fig. 6(c)] for the 1-cm-long WGs with the WG diameter size of around 6 μm is obtained over a large depth range from 300 to 900 μm. Revealing strong dependence of insertion loss on the WG size provides a unique way to improve WG performance in various coupling cases.

The critical issue for the multiscan technique is the relatively low fabrication yield. In addition, the scan speed in the multiscan case is usually the same as that in the single pass scan, and there have been no systematic studies about the optimal speed in the multiscan, uncovering what may enable improvement of the fabrication efficiency with low propagation loss, coupling loss, and bend loss. Our work indicates that monitoring the WG size offers an effective way to optimize the multiscan process

efficiently.[67] Furthermore, the optimal processing window for low-loss WGs is usually small, and the fluctuation in the writing process may be detrimental to the reproducibility and the uniformity, especially when the number of the WGs is larger. Multiscan as well as the aforementioned SLM-assisted parallel writing should be helpful for improving the writing reproducibility and the uniformity.

Besides rescanning the laser along the whole path, tapering the WGs close to the end facet was also demonstrated to be a useful technique to increase the refractive index as well as to enlarge the modification region.[68,72] As shown in Fig. 6(d), a spatial power ramp is used. Multiscan is performed at the last few millimeters of a WG with increasing laser power, ranging from just under the modification threshold up to a moderate power level. Figure 6(g) shows that mode field size can be modified by tapering of WGs with the multiscan. Furthermore, the coupling efficiency to the standard single mode fiber is also enhanced.
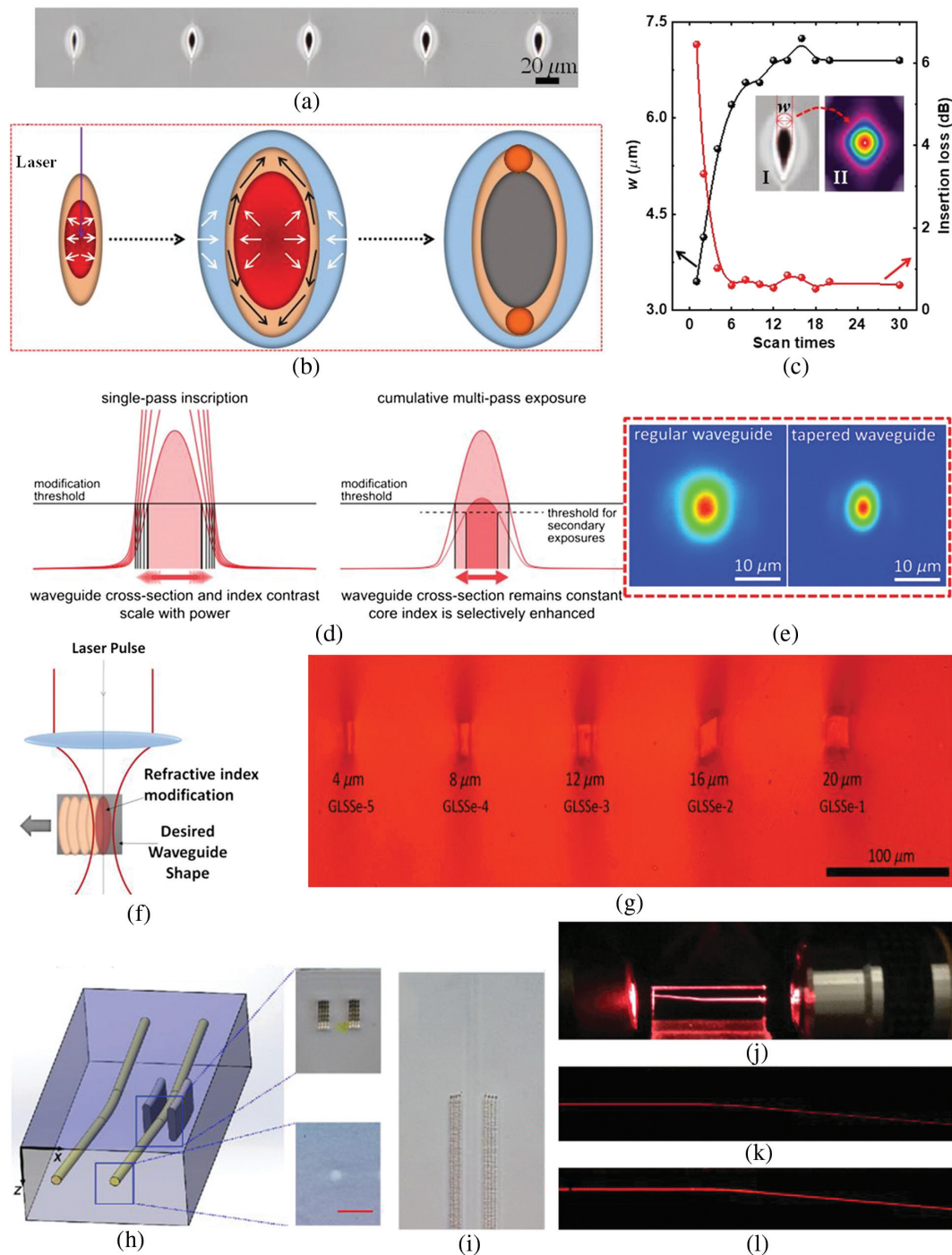
In another case, the WG cross-section is tunable using the multiscan technique, and an offset is adopted between consecutive parallel scans with a small distance in the direction perpendicular to the laser scanning direction, as shown in Fig. 6(f).[69,70,73–76] This technique does not depend on the intensity distribution at the focal volume and enables WG fabrication with desirable morphologies, such as square cross-sections along with a step index refractive index profile [Fig. 6(g)]. The size of the WG cross-section and the change in refractive index can be controlled independently by varying the scan parameters and the translation speed, respectively, and this is not achievable using beam shaping techniques. Furthermore, integrated photonic lanterns constituted with an array of single mode WGs can be produced using the multiscan technique, which have found many applications in astrophotonics and remote sensing.[77–80]

In addition, writing a pair of parallel structures with a desirable distance to sandwich the curved WG will control the stress and birefringence effect in the WGs.[81,82] The refractive index change would increase from 1.85×10^{-3} to 3.45×10^{-3} in the guiding core, as shown in Fig. 6(h).[71] Consequently, the bend loss is suppressed drastically from 2.7 to 0.3 dB for a bend arc angle of 5 deg. A similar technique is adopted to fabricate a mode field compressor and reduce the mode field size.[83] Birefringence is demonstrated to be tunable in the range from 0 to 4.35×10^{-4}, and this allows great flexibility in designing polarization sensitive and insensitive components devices on one single chip, which adds another degree of freedom in the fabrication of integrated optical devices.[81,82]

2.3 Thermal Annealing

Stress can be induced during the WG writing in glass, and anisotropic and inhomogeneous distribution of the refractive index in the modified region is generated through the photoelastic effect, which would lead to a polarization shift and polarization dependent losses as well as an asymmetrical mode field and large propagation loss.[84,85] The stress in the cladding zone surrounding the WG core also reduces the refractive index contrast between the WG core and the outer region, which can cause high propagation loss and bend loss.[86] Thermal annealing has been demonstrated to be a useful method for stress relaxation and complex material reorganization.[82,85,86] In general, heat increases the atom movement rate in the glass matrix by offering the

Fig. 6 (a) Cross-sections of WGs written by scanning fs lasers 1, 2, 4, 6, and 10 times. (b) Schematic view of temperature gradient assistant fs laser writing. Black arrow: matter expansion and flow driven by temperature gradient and stress. White arrows: stress. (c) Insertion loss and diameter (w) of WGs fabricated by scanning various times at 300 μm. Inset: I, cross-section; II, near-field mode profile. Figure reproduced from Ref. 67. (d) Left: illustration of the dependency of the WG cross-section on the fs laser power. Right: cross section of WGs tapered by multiscanning with a low power at the end of the WG. Figures reproduced from Ref. 68. (f) Schematic of the multiscan WG fabrication with an offset perpendicular to the writing direction. Figure reproduced from Ref. 69. (g) Size variation with an increase in the number of scans. Figure reproduced from Ref. 70. (h) Schematic of the sandwiched WG. Insets: the cross sections of the WG and bend-loss-suppression walls. Scale bar: 30 μm. (i) Top view of the sandwiched WG. (j) A 633-nm laser beam propagating in the WG. Top view images of a WG bend (k) without and (l) with bend-loss-suppression walls. Figures reproduced from Ref. 71.
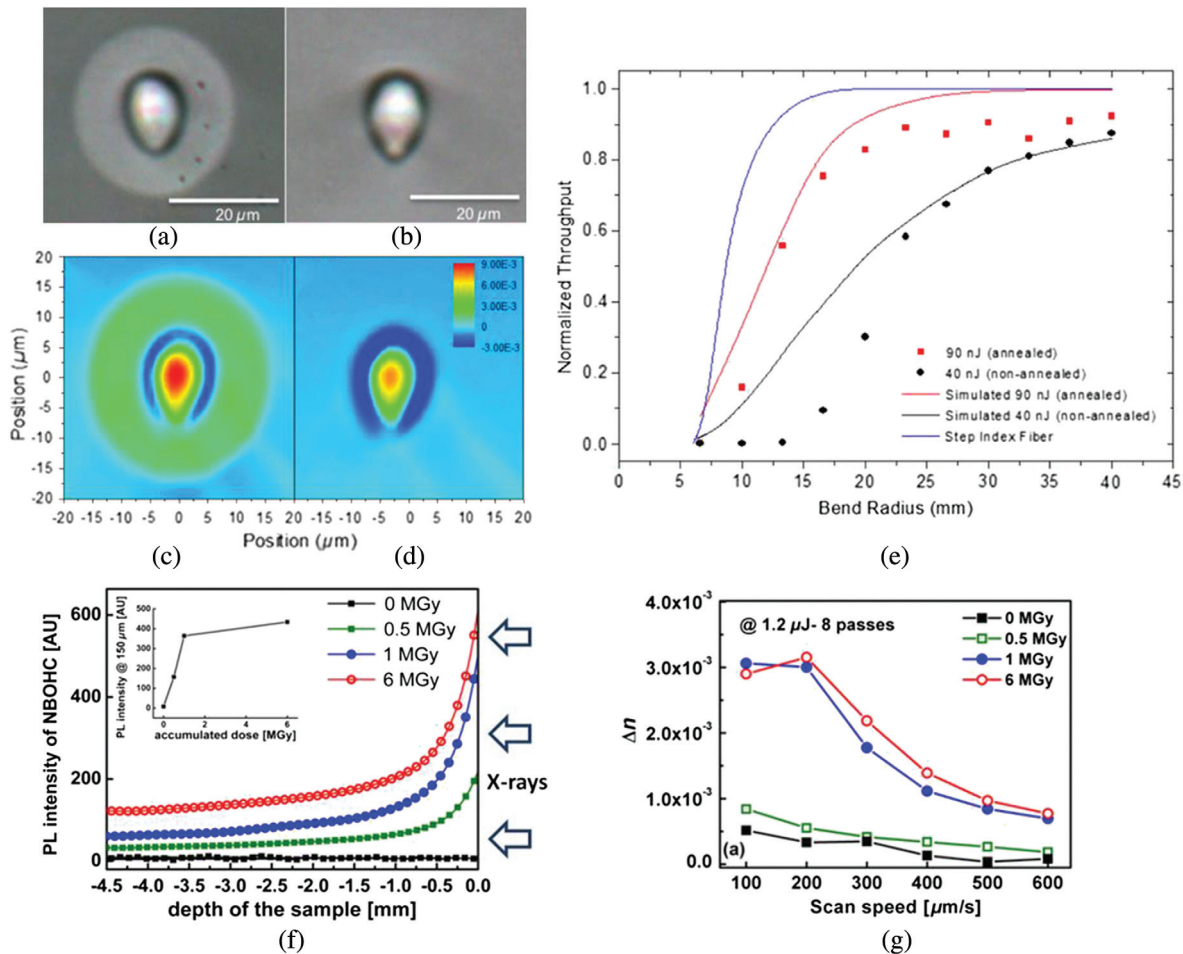
energy for breaking bonds and during annealing at temperatures in the vicinity of the glass transition temperature, where the formation of new bonds and structural rearrangement may have occurred, which leads to a decrease in the structural inhomogeneity.[87–89] As a result, the reduction of the structural deformation leads to stress relaxation. In addition, nonbridging oxygen hole center (NBOHC) defects can also disappear at low temperature (e.g., 300°C for silica glass).[33,90] Consequently, the size of the guiding core and the structure anisotropy are reduced, the refractive index contrast in the core/cladding regions increases, and these are accompanied by lower propagation loss and bend loss along with higher mode symmetry.

A typical rate thermal annealing process is adopted for this purpose. The key characteristic of this thermal treatment is the slow cooling rate that enables removing the stress and birefringence effectively. In general, to initiate an erasure and stabilization process, the sample is initially heated above the transformation temperature. Once reaching the maximum temperature that is well below the softening temperature of the glass, a very slow cooling rate is adopted until the glass temperature is cooled down below the strain or transformation point temperature.[82,86] Figures 7(a) and 7(b) show the cross-section

of the WGs before and after annealing, respectively, and the refractive index profile is displayed in Figs. 7(c) and 7(d), respectively, which clearly indicate that the outer lower refractive index zone is removed by thermal annealing. As a result, the output power through the WGs increases, and the bend loss decreases significantly, as revealed in Fig. 7(e). Symmetric polarization-insensitive WGs are also available with ultralow birefringence and low propagation loss of 0.3 dB/cm. Babu et al. also reported that insertion loss could be reduced effectively to 1.01 dB at 632.8 nm by an isochronal annealing treatment, which is due to the bleaching of the NBOHC defects.[91,92]

2.4 Predefect Engineering

One of the big challenges for direct writing of WGs by fs lasers is the increase in the refractive index of WGs, which would foster better performances of the devices. As the presence of defects makes great contributions to the refractive index increase, predefect engineering of materials to induce an incipient defect density has been explored to cause an increment in the refractive index.[34] The predefects can be generated by hard (40 keV) X-ray irradiation with accumulated doses up to

Fig. 7 Cross sections of the WGs (a) before and (b) after thermal annealing. Refractive index profiles of WG (c) before and (d) after annealing. (e) Normalized output through the WGs as a function of bend radii. Figures reproduced from Ref. 86. (f) PL intensity versus depth in the glass after X-ray exposure with various doses. (g) Change of refractive index (Δn) in the WGs as a function of the scan speed at different X-rays doses. Figures reproduced from Ref. 34.

6 MGy, which subsequently serve as precursors for further defect generation induced by fs lasers, along with an overall increase in photosensitivity. As a result, photoinscription efficiency is enhanced, and a higher index change is obtained. Figure 7(f) shows that the PL coming from NBOHC increases with an increase in X-ray doses from 0.5 to 6 MGy, especially in the depth smaller than 500 μm, and the unexposed sample does not emit PL, which indicates the generation of NBOHC after X-ray irradiation. The increase in refractive index is much larger with 1 and 6 MGy doses of X-ray irradiation than that with 0–0.5 MGy doses of irradiation at all scan speed, as shown in Fig. 7(g). In conclusion, predefect engineering is a promising technique to increase the refractive index of WGs, which also enables validating scenarios of defect-assistant densification for the refractive index change. Furthermore, we suggest that UV light or electron and ion beam preirradiation may also lead to similar effects, and further experimental work is needed to verify this proposal.[93,94]

2.5 Composition Engineering

As the optical properties and photoresponse to fs lasers depend on the chemistry of glass, and the fs laser-induced refractive index change would be determined by the structural and elemental reorganization, composition engineering is a simple and promising alternative route to improve the performance of written WGs in glasses, especially in the thermal writing regime with high repetition rate lasers.[95–98] In the fs laser writing process, the local temperature would be higher than that of the softening and working point of glass.[67,98] As a result, the breaking of bonds linking the network modifiers or the network formers will occur in this high-temperature field, and the ions, including O^{2-}, would diffuse and modify the local compositions of glass, which usually leads to formation of two typical zones with positive and negative refractive index change, respectively. Increasing the concentration of the components such as Ca, La, and Al that induce densification and disorder causes a larger increase in refractive index, with Δn reaching 10^{-2}, and reduces the coupling loss and propagation loss significantly.[96,97,99] For example, in typical alkali-free borosilicate glasses, such as Corning Eagle 2000, Corning Eagle XG, and Schott AF32 glasses, the characterizations based on the refractive index mapping, electron microprobe analysis, and Raman spectroscopy clearly suggest that an increase in the concentration of the silicon element causes a decrease in refractive index, and an increase in the concentration of Ca and Al elements leads to an increment in the refractive index.[96] Similar phenomena are also found in other glass systems.[97] Germanium doping in silica glass is suggested to increase the refractive index change.[100] The increment in the concentration of Al_2O_3 in the aluminosilicate glasses could lead to breaking of the Si-O-Si network into four and three-membered ring structures accompanied by structure densification, which is confirmed by the increase of Raman intensity at D_1 (∼485 cm^{-1}) and D_2 (∼600 cm^{-1}) peaks.[91] The presence of silver was reported to decrease the insertion loss of the WGs in the binary tellurite-zinc glass, but the mechanism is still unclear.[101] However, although composition engineering is a useful method to increase the refractive index change, there have been not as many efforts to optimize the compositions and controll the element migration in a desirable way for achieving better performance, and more systematical studies are still needed.

3 Applications in Optical Coupling and Integrated Devices

WG writing by fs lasers in glass has found various applications in a vast range from scientific researches to technological devices.[14,15,102–107] In this review, we focus the recent progress in the WG applications for photonic integrated devices in communication, topological physics, quantum information processing, and astrophotonics.
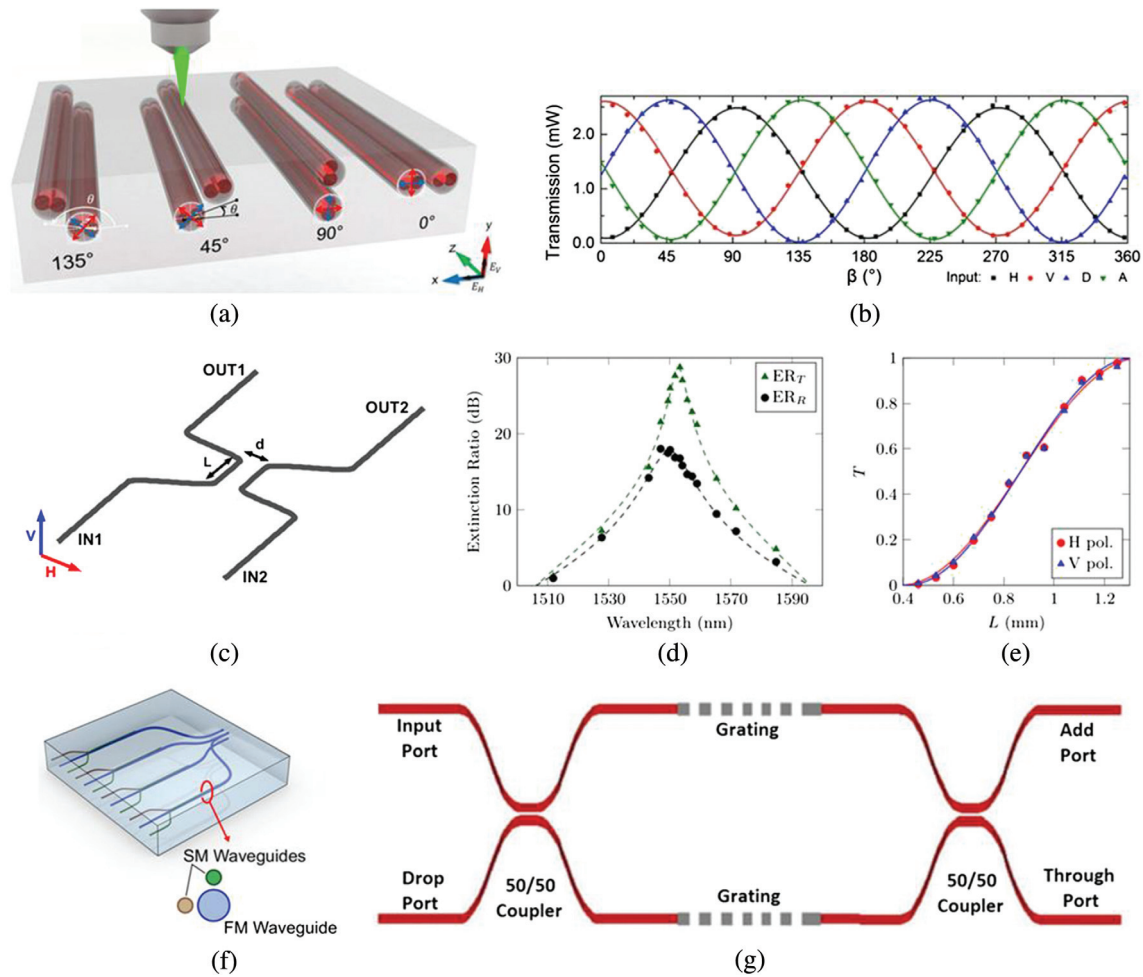
3.1 Optical Couplers and Network Devices

Optical couplers are one of the key building blocks for combining and splitting optical signals in photonic integrated circuits.[2,108] A compact, low-loss, broadband power coupler with polarization sensitivity or insensitivity is highly required for many applications, such as power splitters, optical switches, multiplexers, directional couplers, birefringent retarders, and rotated waveplates.[43,68,82,102,105,108–110] The flexibility in photonic circuit configuration and mass production with designability in 3D helps WG writing by fs lasers to build couplers and splitters with arbitrary shapes and tunable coupling ratios in glass.[104,105,111] Especially, achieving polarization transformation is achievable and also desirable in integrated architecture with WGs created by FLDW, and this is critical for quantum applications, as controll over polarization enables performing operations with polarization-encoded photonic qubits.[43,111–113]

For example, an on-chip rotated polarization directional coupler (RPDC) operating at 780 nm with an arbitrary birefringent optical axis can be constructed via writing a double-track, as shown in Fig. 8(a), through which the distribution of the refractive index between adjacent tracks in the fused silica is tuned.[43] In this case, a single-mode WG with an artificially birefringent optical axis and high transmittance could be produced by adjusting the relative radial and azimuthal positions of the tracks. Figure 8(b) shows the polarization analysis of the 45-deg rotated birefringent optical axis measured by two crossed polarizers. The visibility of the input polarized light propagating along the optical axis remains as high as 98% to 99%. Characterization of the transmission power of the 45-deg RPDC with adjusted coupling lengths indicates that coupling lengths are the same for the 0-deg and 45-deg RPDCs, and the parallel coupling length could be determined to be 23 mm. Reconstruction of the Stokes vector was also performed, and the average fidelities reach 98.1% and 96.0% for the 0-deg and 45-deg RPDCs, respectively, with the corresponding average ratios up to 16 dB (0 deg) and 20 dB (45 deg).

Shortening the distance between the coupled WGs in the couplers may induce strong anisotropic mechanical stress, which was exploited to decrease the size of the polarizing directional couplers down to 3.7 mm with WG distance below 5 μm.[116] Importantly, the WGs exhibit low birefringence out of the coupled region. As a result, this approach allows for constructing complex polarization-sensitive integrated circuits with high integration. The extinction ratios at the operation wavelength of 808 nm are determined to be about 16 and 20 dB for the horizontal and vertical polarizations, respectively.

Polarized and polarization insensitive directional couplers, working in the telecom band of 1550 nm, were also fabricated in aluminoborosilicate glass (EAGLE, Corning) just by controlling the interaction length (L) and the separation of two WGs (d), as shown in Fig. 8(c).[111] This paves the way to the integrated

Fig. 8 (a) Illustration of the double-track approach for fabrication of WGs and RPDCs. θ is the geometrically radial and azimuthal offset between two adjacent tracks (dark red) in each WG (gray). (b) Polarization analysis of the 45-deg rotated parallel coupling region with different linear input states [H, V, antidiagonal (135 deg, A Pol.) and diagonal (45 deg, D Pol.)]. Figures reproduced from Ref. 43. (c) Schematic of a DC. Two input (out) ports: IN1 and IN2 (OUT1 and OUT2). (d) Transmission and reflection extinction ratios for a PDC with L of 33.2 mm and d of 12.5 μm in the telecom band. (e) Transmission for polarization insensitive DCs with L of 0.4 to 1.3 mm and d of 8 μm. Figures reproduced from Ref. 111. (f) Diagram of the 4-core few-mode coupler. Figure reproduced from Ref. 114. (g) Schematic of the optical add-drop multiplexer configuration. Figure reproduced from Ref. 115.

controll over polarization encoded photonic qubits and polarization entanglement at the 1550 nm wavelength range. In general, the WG birefringence causes a different periodicity for different polarization states in the power oscillation between the two WGs in the DCs, which can be described as

$$T = \sin^2(kL + \emptyset_0), \quad R = \cos^2(kL + \emptyset_0), \quad (11)$$

where T is the power transmission coefficient, R is the reflection coefficient, k is the coupling coefficient between the optical modes, and $\emptyset_0$ is an offset for the coupling occurring in the curved segments incoming and departing from the coupling region.

Large phase difference could be present with large L. With the appropriate coupler geometrical and coupling parameters, the two oscillations can be in antiphase, which results in a

polarized DC. For example, Fig. 8(d) shows that the extinction ratios between the two polarizations are higher than 25 dB at 1550 nm with extinction ratios higher than 15 dB, where L is 33.2 mm, and d is 12.5 μm. While for shorter interaction lengths, the DC exhibits polarization insensitivity. Figure 8(e) shows the transmission for DCs with L of 0.4 to 1.3 mm and d of 8 μm, and the absolute transmission difference for the two polarizations is as low as 10^{-4}, meaning polarization insensitivity. The authors suggested that the alteration of the optical properties caused by the inscription of the second WG to that of the first one in the coupler is the origin of such polarization-insensitive behavior. Techniques, such as birefringence compensation and thermal annealing, were used to improve the symmetry of the WGs and the birefringence, which lead to symmetric polarization-insensitive DCs.[82] These achievements imply that it is possible to integrate polarization

dependent and independent devices in a single circuit by just manipulating the geometrical parameters of the components, which will be vital in future complex photonic devices.

To realize arbitrary photonic waveplate operations on chip, a stress engineering technique via writing an additional modification track near the WG was adopted to create an artificial stress field and rotate the optical axis of the birefringent WG.[108] Higher pulse energy and lower writing velocity were used for writing the second defect track, in which no light propagates. Consequently, Hadamard, Pauli-X, and rotation gates for encoding photonic polarization qubits on chip were achieved with high fidelity on both classical and quantum states of light. In this case, the retardation between ordinary and extraordinary field components was tuned, including half-wave plate and quarter-wave plate operations through modifying the length of the modified track parallel to the WG.
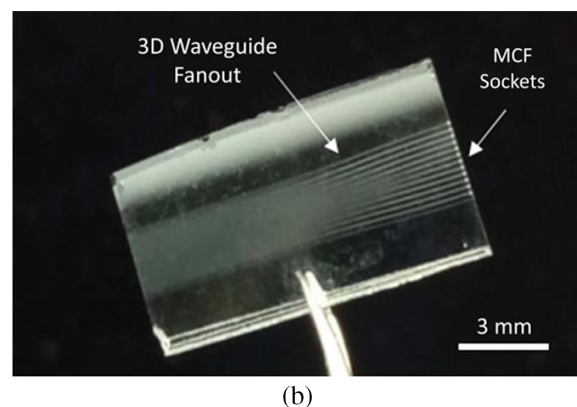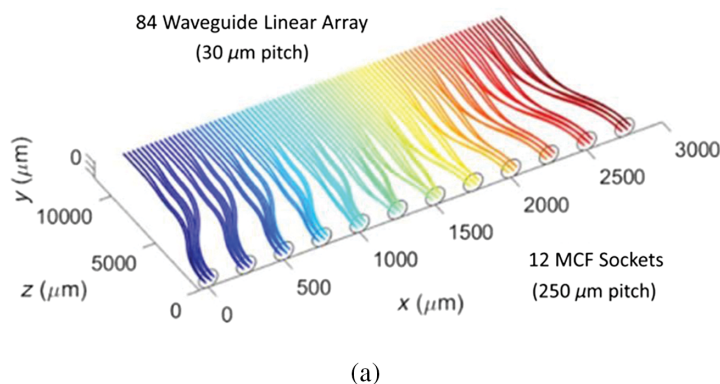
Furthermore, to support the ever-growing demand in transmission bandwidth and capacity over a communication channel, a number of technological features have been developed by the telecommunication community in the past decades.[117] 3D multiplexers and demultiplexers based on WGs were produced and could be integrated on a photonic chip.[19,68,102,114,118,119] Ultrahigh capacity space-division multiplexers systems were built in borosilicate glass.[19] For example, 1.2 Pb/s throughput transmission was demonstrated using the few-mode multicore fiber (four-core, three-mode) with a cladding diameter of 160 μm, as shown in Fig. 8(f).[114] In this case, 368 wavelength division multiplexed spatial super channels across the C and L bands were used. Simultaneous multiplexing of the LP_{01}, LP_{11a}, and LP_{11b} modes of all cores is achievable in this three-mode, four-core fiber with high mode extinction ratios and low insertion losses over a large bandwidth across the S + C + L bands.[111] In addition, optical add–drop multiplexers written in fused silica were demonstrated operating at 1550 nm, as shown in Fig. 8(g).[115] To this end, two DCs with a symmetrical geographical layout were used in a Mach–Zehnder interferometer configuration for the signal routing, and the inserted Bragg grating WGs between the DCs worked for wavelength selectivity. In principle, the input signal is split equally into two WGs by the first DC, which is then guided to two identical Bragg grating WGs. The resonant wavelength is reflected to the drop port and collected. The remaining transmitted signal will leave from the through port. New information at the resonant wavelength can also be added

to the output signal through the add port. The versatility of the fs writing technique promises the capability of scalable DM fabrication with more modes and cores and mass production. As a result, practical ultrahigh capacity dense space-division DMs are expected.

Due to the intrinsic flexibility of 3D fabrication, WG-based fan-out devices were also achieved, with one end consisting of a 1D WG array and another end consisting of a 2D WG array, which can be used as multiplexers, demultiplexers (aforementioned), interposers to interconnect silicon photonic chips, as shown in Fig. 9(a), and astrophotonic interferometer integrated chips (discussed later).[78,79,121] For example, WGs in a glass interposer were reported to vertically couple light from an optical fiber to the silicon photonic chip.[122] An 84-channel interposer is also realized for coupling a multicore optical fiber and silicon photonics chips, as shown in Fig. 9(b).[120] However, misalignment causes significant loss in the packaging and stabilizing process. Further improvement in the packaging step for edge coupling of WGs to the silicon photonic chips is one of the biggest challenges. For the future, the optimized 3D WG fan-out devices may promise an attractive balancing of loss, mode matching, high channel density, low crosstalk, and multifunctional integration with other photonic components.

3.2 Topological Physics and Quantum Information Processing

In the past decades, photonic structures consisting of arrays of evanescently coupled WGs have emerged as a major representation of functionalized optical structures, in which the light propagates along the topological states or the light evolution exhibits intrinsic similarities with the quantum evolution of particle wave-functions. As a result, WG arrays have been proposed as a typical model system for researches and applications in topological physics and quantum information processing, such as formation of topological edge states, quantum mechanics emulation, and quantum computing. FLDW has been established as a standard method to construct 3D WGs into a variety of optical bulk materials, which enables the achievement of various innovative topological states, quantum physical concepts, and quantum information applications that are not feasible with other fabrication techniques.[2,14,123,124]
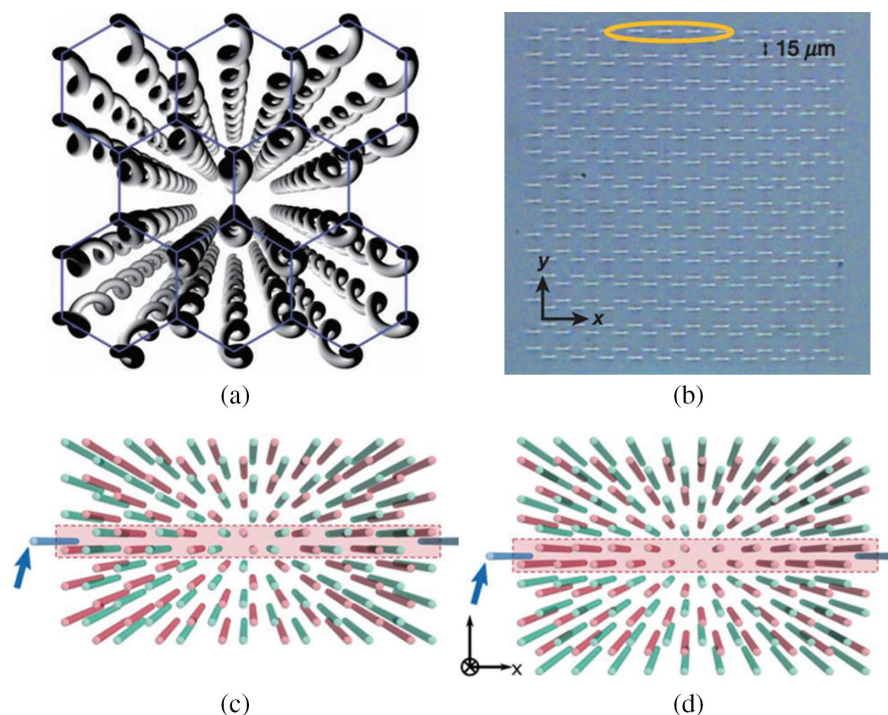

(a)

(b)

Fig. 9 (a) Schematic for an 84-channel interposer in glass, fanning out from a linear array (silica photonic chip at back) to 12 socket positions for multicore fibers (MCFs) packaging. (b) Optical image of the interposer in silica glass. Figures reproduced from Ref. 120.

Recently, the rise of topology has been one of the most recognizable trends in physics.[125,126] In the topological phases, protected travel is allowed along the edges of the structures in a robust way, giving rise to immunity against backscattering by defects. In particular, topological photonics have attained a burst of interest, as light waves can work as a platform for revealing the nontrivial bulk and edge topological states by carefully structuring photonic crystals.[125–127] WG photonic lattices are frequently adopted to build photonic topological structures for investigating the interplay of topology and interparticle interactions.[128–131] For example, the helicity of the evanescently coupled helical WG array would break the z-reversal symmetry in a honeycomb photonic lattice [Figs. 10(a) and 10(b)], which leads to formation of Floquet topological insulators, and topologically protected transport of visible light is observed on the lattice edges.[127] Photonic Floquet topological insulators in the fractal lattices were proposed theoretically, and robust travel along the outer and inner boundaries of the fractal lattices without scattering was possible.[133] Experimental realization of topological fractal insulators is promising. Solitons were also identified in an anomalous photonic Floquet topological insulator, which exhibited different behavior in that they executed cyclotron-like orbits.[134] For this purpose, the WG lattice was modulated periodically along the axis, and this resulted in a nonzero winding number with the optical Kerr effect-induced nonlinearity. The observation of topological solitons offers new prospective directions for the topological nonlinear optics, complementing other platforms. 2D honeycomb photonic lattices with broken inversion symmetry were also reported to exhibit photonic topological valley Hall edge states and four-

dimensional (4D) quantum Hall.[132,135] Detuning the refractive index of the two honeycomb sublattices with varying average writing pulse energy of the fs laser generates an armchair [Fig. 10(c)] and zigzag edges [Fig. 10(d)] at their domains and a boron nitride-like band structure.[132] Consequently, the edge states appear along the domain walls between regions with opposite valley Chern numbers. The valley-Hall effect enables a new mechanism for realizing time-reversal-invariant photonic topological insulators. The fabricated time-reversal invariant WG photonic lattice could possess a zero-dimensional topological defect corner mode, which represents a new type of crystalline topological phase with a topologically protected energy lying at mid-gap and insensitive to disorder.[136]

In addition, sufficiently strong disorder can lead to the close of the topological bandgap, and the system becomes topologically trivial with all states being localized and all transport vanishing, complying with Anderson localization [Figs. 11(b) and 11(e)]; but, adding on-site disorders with random variations in the refractive index of WGs could drive the system from a trivial phase into a topological one, resulting in the emergence of topological Anderson insulators with protected edge states and quantized transport, as revealed in Figs. 11(c) and 11(f). In this case, the refractive index detuning was induced by adjusting the writing speed during the fabrication process, and a slower writing speed leads to a larger refractive index in WGs. The topological Anderson insulator was demonstrated experimentally with sufficiently detuned honeycomb photonic structure of helical WGs.[137] The light propagates only along the edge in the Floquet topological insulator [Fig. 11(d)]. When there is strong disorder, the system becomes topologically trivial, and there is

(a)

(b)

(c)

(d)

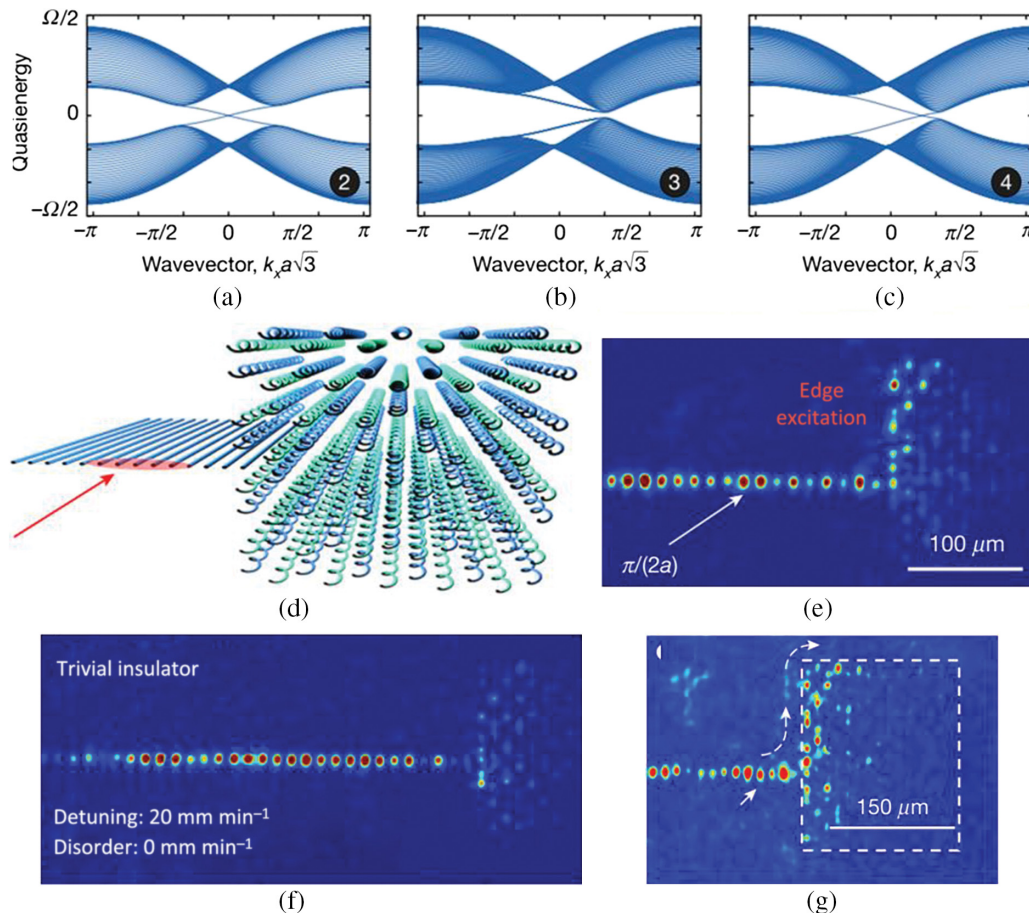**Fig. 10** (a) Sketch of the helical WGs with honeycomb geometry. (b) Optical image of the input facet of the photonic lattice. Figures reproduced from Ref. 127. Schematic diagram of honeycomb lattices with (c) armchair and (d) zigzag edge domain walls. Red and green WGs exhibit a different refractive index, and blue is the excitation WGs. Red-shaded regions are domain walls. Figures reproduced from Ref. 132.

no light along the edge [Fig. 11(e)]. After introduction of sufficiently strong on-site disorder, a photonic topological Anderson insulator is generated, which is confirmed by the presence of the mid-gap excitation-induced coupling to a topological edge state, as shown in Fig. 11(f). A photonic topological insulator in a synthetic dimension with topological edge states was demonstrated successfully.[138] In this case, a 2D WG array was produced with 1D in real space and one synthetic dimension in modal space. As a result, the propagation of the topologically protected edge state was observed at the edge of the synthetic space, but not at the spatial edges of the system. Waveguiding by artificial gauge fields was demonstrated using an array of evanescently coupled identical WGs. In this realization, WGs in the core and cladding follow distinct trajectories during propagation, and the artificial gauge field caused a shift of the dispersion relations from one another in the core and in the cladding in momentum-space.[139]
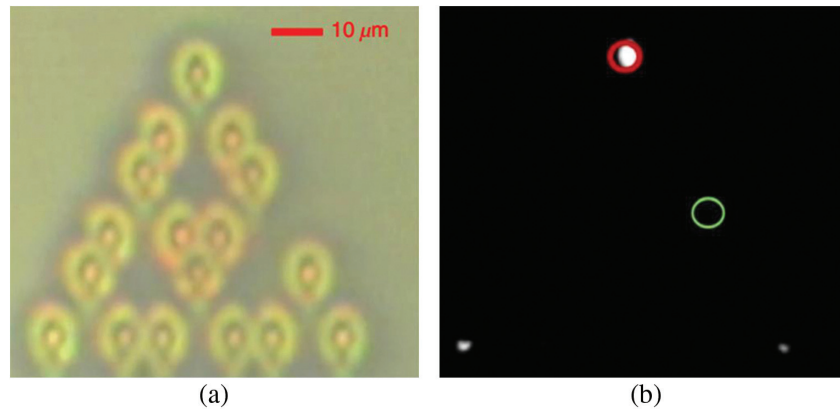
In contrast to the intricate set-ups with helical optical WGs [Fig. 10(a)], Fig. 12(b) indicates the presence of kagome-based corner states in the straight WGs, which exhibit a high degree of flexibility and control, operating in the visible light range.[140] Furthermore, topological boundary states in a single photon level were established in the WG-based quasicrystal, with the protected topological phases against the decoherence caused by diffusion and the noise.[141]

Quantum computing and quantum communication offer high efficiency in approaching problems of scientific and commercial interests, where processing an extremely large amount of data with fast speed is on-demand.[142,143] Photonic WG lattices give rise to an excellent model system allowing for simulating many quantum statistics for quantum information processing.[144,145] For example, boson sampling experiments against various alternative hypotheses were achieved on larger WG photonic chips fabricated by fs laser writing, which will be critical for boson sampling devices to conform the supremacy of quantum information processing over classical computers.[124] Anderson localization of a pair of noninteracting entangled photons was observed in an integrated quantum walk by employing

Fig. 11 (a) Topological bandgap for the Floquet topological insulator in a helical honeycomb lattice. (b) Breaking the parity structure symmetry by detuning the sublattices with formation of a trivial bandgap. (c) Forming topological Anderson insulator phase by suppressing the effect of the parity-symmetry breaking terms with sufficiently strong disorder. (d) Hybrid structure with a 1D straw and a 2D honeycomb helical WG lattice. The excited state was controlled by the "straw"—through which the modes of the system were selectively excited. Excitation light along the edge states in the (e) Floquet topological insulator, (f) trivial insulator, and (g) topological Anderson insulator. The input positions were indicated by the white arrows. Figures reproduced from Ref. 137.

Fig. 12 (a) Triangular photonic lattices with a defect in a straight WG array. (b) Observation of the "fractionalized" corner states. Red circle: injection of 720-nm coherent light into the WG at the corner indicated. Green circle: missing WGs. Figures reproduced from Ref. 140.

polarization entanglement of photons to simulate the quantum statistics in the WG arrays.[146] Genuine many-particle quantum interference and high-visibility quantum interference of single-photon topological states were observed with the fs laser written integrated photonic circuit.[145,147] Two topological edge states were brought into proximity, interfering and undergoing a beamsplitter operation, and the visibility of the Hong–Ou–Mandel interference is as high as $93.1\% \pm 2.8\%$.[147] By integrating a quantum dot-based multiphoton source and a WG photonic chip in glass, scalable platforms exhibiting high-rate many-particle quantum interference were attained.[148] Jin and coauthors reported a 2D continuous-time quantum walk with a single photon on the 2D WG array and quantum fast hitting on hexagonal WG photonic structures with up to 160 nodes and a depth of 16 layers [Figs. 13(a)–13(c)].[149,151,152] They showed that the time for optimal quantum hitting increases linearly with network depth, as shown in Fig. 13(d). In comparison, Fig. 13(d) indicated that classical random walk was characterized by a quadratic relation. As a consequence, quantum speed-up to improve information processing is highly promising, which would initiate breakthroughs into real-life applications. Recently, a scalable photonic computer was developed to solve the subset sum problem. Photons were found to dissipate into the photonic circuits and search for solutions in parallel that result in an exponential superiority over even supercomputers in time consumption, as shown in Fig. 13(e).[150] Furthermore, quantum polarization entangled states could be well topologically protected on a photonic chip, and the linking of photonic topology and quantum information opens the door to topological enhancement in the quantum regime.[153]
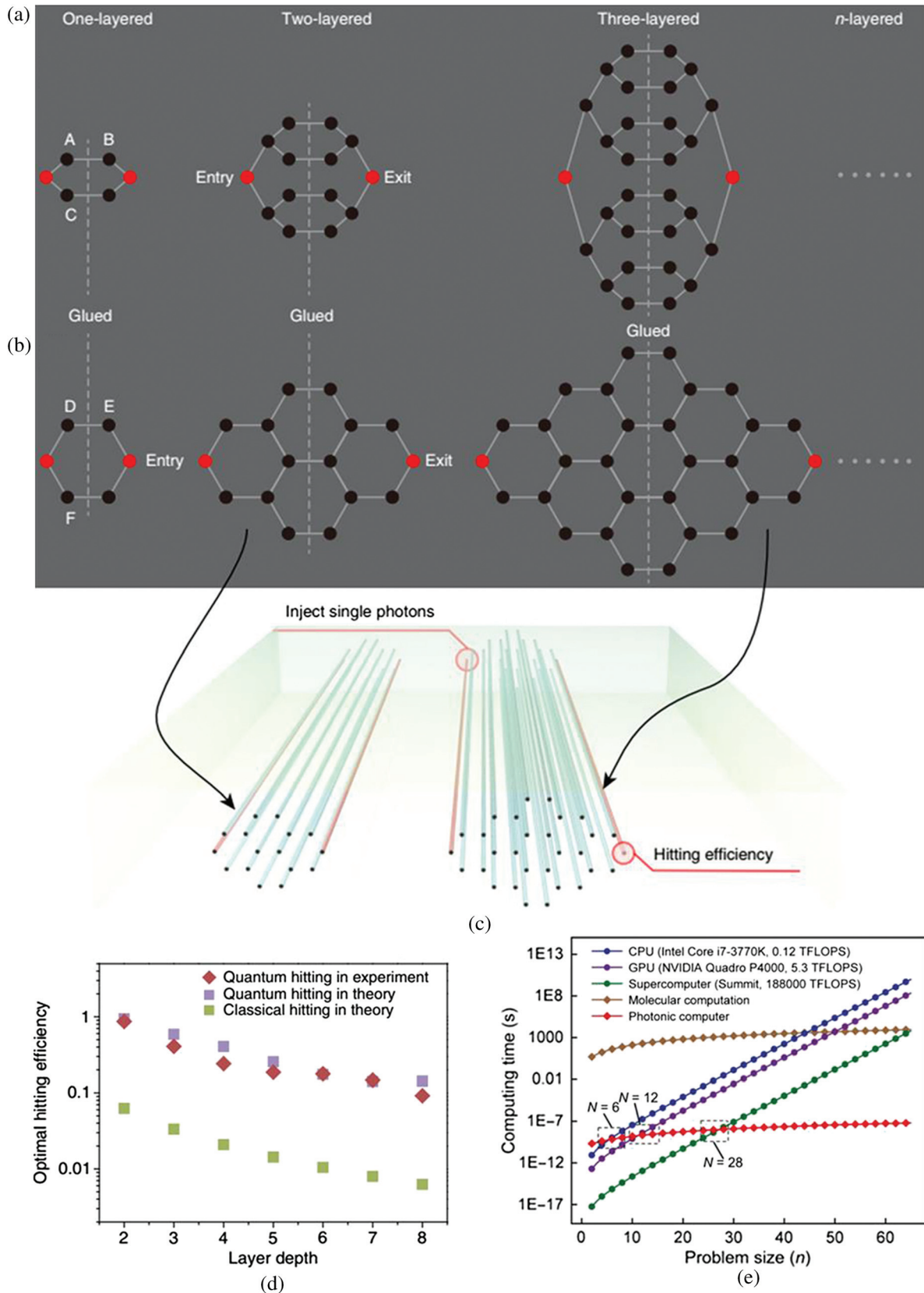
Many other applications in the photonic topology and quantum information processing were also reported. For example, using the fs laser written 3D helical WG lattices, type-II Weyl points of light at optical frequencies were observed experimentally, confirmed by the presence of conical diffraction with the frequency corresponding to the Weyl point, and Fermi arc-like surface states.[154] A Weyl exceptional ring was also realized with the upper and lower bands of the topological transitions meeting at a ring, rather than a point, by observing the lack of conical diffraction at the topological transition when the system is non-Hermitian with quantized Berry charge.[155] A scalable approach for the operation of the fast Fourier transform algorithm was developed using 3D WG photonic integrated interferometers.[156] Unique complex photonic quantum structures, such as the fractal network, can be built with 3D fs laser writing, which provides platforms for the investigations about the properties of these structures.[20]
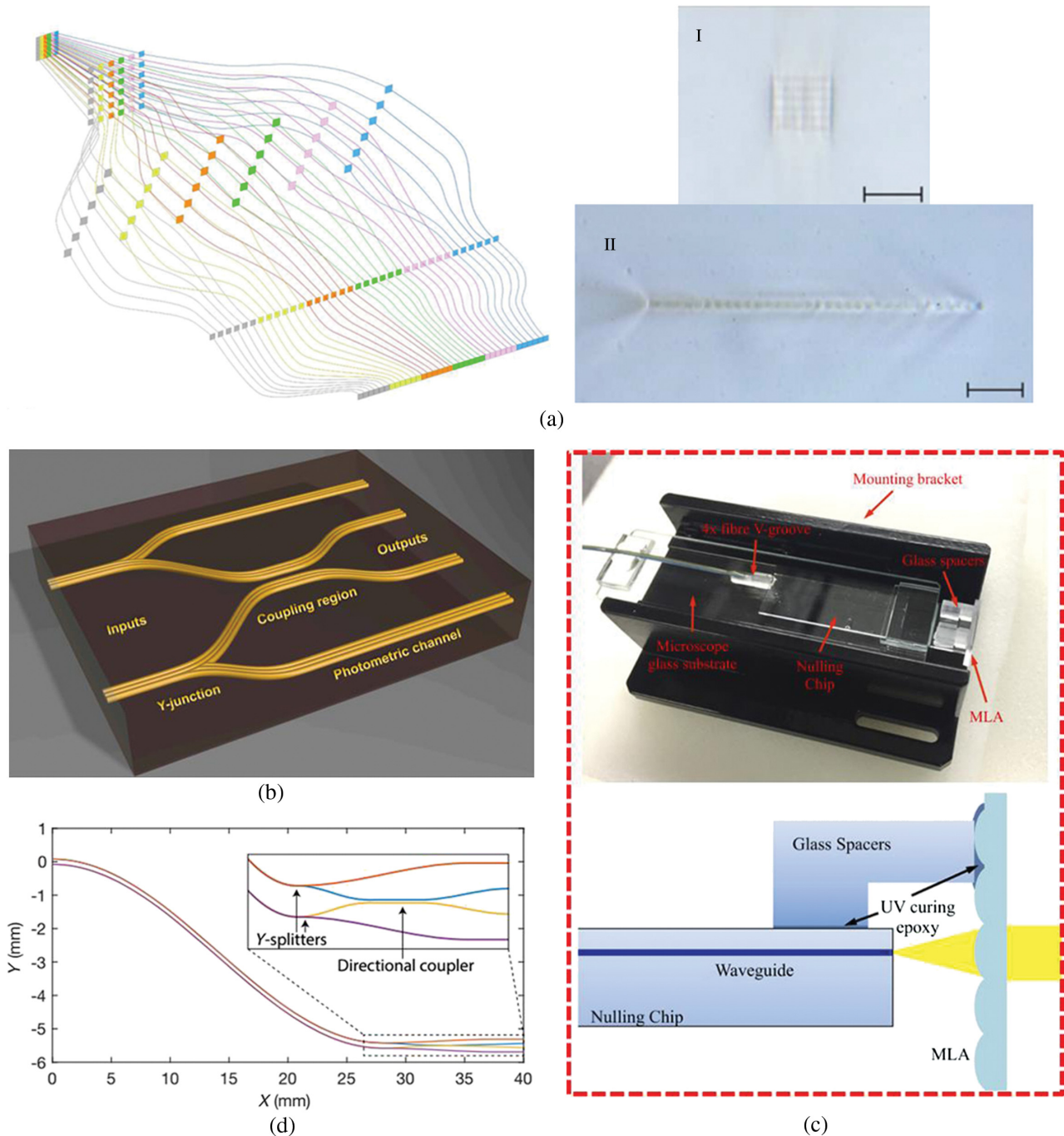
3.3 Astrophotonics

Application of fs laser writing WGs for astrophotonics was proposed in 2009 by Thamson et al., which relies on the capability of 3D designability with high WG density and precision position control.[77] Implementing various optical functions on a single integrated chip enables the reduction of the complexity of traditional astronomical instruments significantly. The typical glass systems for astrophotonics include silica glass, borosilicate glass, chalcogenide glass, and fluoride glass.[78,80,157–164] For the demonstration, integrated photonic lanterns were fabricated, which can couple multimode light to an array of single-mode WGs.[78] These integrated devices [named photonic dicers, as shown in Fig. 14(a)] are also developed as a diffraction limited pseudoslit and used to reformat multimode light into a 1D array for high-resolution diffraction limited spectroscopy.[158–160,165] In this case, multimode light collated from the telescope (I in Fig. 14) is spatially overlapped, and the input modal noise is converted into amplitude and phase changes along the slit, which minimizes the slit length as well as the number of detector pixels for light analysis in the spectrograph. However, during on-sky testing, wavelength-dependent loss was discovered, which manifests as modal noise and makes it difficult to extract and calibrate spectra properly.[160] By integrating WG S-bends, Y-splitters, and directional couplers on one chip, as shown in Fig. 14(b), nulling interferometers were written in gallium lanthanum sulfur (GLS) glass via multiscans of 5.1 MHz fs laser.[162] In this two-port interferometer, the Y-splitters direct half of the light into the outer photometric channels, with another half directed into the two inner channels for interferometric interaction. The starlight is nulled by destructive interference in the coupling region. The remaining light at the output of the coupler may originate from a possible exoplanet near the star. On-sky demonstration was also realized with the nulling interferometer integrated in the borosilicate glass [Fig. 14(c)].[80] In this chip, each WG encountered a Y-splitter with 33% of the light split off that was sent to separate

Fig. 13 Schematic diagrams of (a) a photonic-chip-based glued binary tree, (b) the proposed hexagonal WG photonic chips, and (c) the quantum fast hitting experiment on the WG photonic chips. (d) Optimal hitting efficiency for hexagonal photonic chips at different layer depths. Figure reproduced from Ref. 149. (e) The estimated computing time for the photonic computer and other competitors. Figure reproduced from Ref. 150.

(a)

(b)

(d)

(c)

Fig. 14 (a) Schematic of a photonic dicer consisting of the 3D WG lattices combining photonic lantern and reformatting functions. I: multicode input end with 6 × 6 array WGs in 2D; II: pseudoslit output end with 36 array WGs in 1D. Figures reproduced from Ref. 159. (b) Schematic of an on-chip two-port nulling interferometer chip in GLS glass. Figure reproduced from Ref. 162. (c) The photonic assembly includes the nulling chip, the microlens array (MLA), and fiber V-groove. (d) The WG arrangement in the photonic chip. Figure reproduced from Ref. 80.

photometric outputs, as shown in Fig. 14(d). An evanescent directional coupler was created by bringing two input WGs together, and it produced a 50:50 splitting ratio at its two output ports. At the output face, the four WGs were butt-coupled and bonded to a fiber V-groove using UV curing adhesive and sent via single-mode fibers to the photodetectors. A periodic 3D array of WGs is also an excellent platform for light coupling

and performing interferometry of the light that comes from telescopes.[157,161,166]

Though laboratory testing and on-sky testing have indicated that the integrated WGs written by fs lasers hold great potential in astrophotonics, there are still some issues hindering their wide application. For example, chalcogenide and fluoride glasses are fascinating alternatives for mid-infrared optic

detecting in the range from 2 to 5 μm, which are in high demand for high angular resolution astrophotonics. Unfortunately, the loss performance of WGs in these mid-infrared glasses (e.g., propagation loss >0.2 dB/cm in chalcogenide glass and >0.3 dB/cm in fluoride glass) is worse than that in silica and borosilicate glasses (that <0.2 dB/cm).[162–164] In fact, the propagation loss will increase in the 3D WG lattices. Second, it is also still difficult to fabricate 3D WG arrays with identical waveguiding performance in each one, especially when the WG number and depth variation are large. As a result, there is a difference between the outputs from different WGs. Beam shaping techniques as discussed above with critical controlling over the writing parameters should be important for writing identical WGs for reliable results and high reproductivity.[40] Third, an oil immersion objective with 1.25 NA is usually necessary for writing loss WGs in mid-infrared glass. As a result, special care should be taken to prevent oil boiling, and the writing depth is also limited. In addition, multi-scan is usually adopted for the astrophotonic WG writing with a tunable size of cross-section. Modified alternative techniques (e.g., temperature gradient-assisted fs laser writing) may be helpful to fabricate optimal WGs under more mild conditions for astrophotonics. Fourth, although the laboratory testing implies that WGs in the mid-infrared glass will be a better choice than that in borosilicate glass for the astrophotonic interferometer, the on-sky demonstration has only been achieved in the latter glass until now. Further work is needed to reduce the loss (including propagation loss, coupling loss, and bend loss) of WGs in the mid-infrared glass for the astrophotonic interferometry.

4 Conclusions and Prospects

The far-reaching goal of on-chip multifunctional photonic circuits is to perform complex tasks within a single chip. Though great progress has been made in developing improved techniques and achieving device applications, besides the aforementioned issue, there exist some potential challenges for the practical applications of fs laser writing WGs. For example, the mechanism of RI change induced by fs lasers is still not fully understood. As a result, optimizing the loss performance usually relies on the experimental experience, and the reported optimized laser parameters are varied from different groups. Uncovering the process of fs laser–matter interaction and mechanisms of refractive index change is urgent and also essential to enhance reproductivity of high-performance WGs. Second, although writing low propagation loss (∼0.2 dB/cm) WGs in borosilicate glass is realized with the high speed of 1 to 10 cm/s, the optimized scanning speed for achieving typically low propagation loss of ∼0.3 dB/cm in silica glass is usually 50 to 200 μm/s, and the effective speed is even much smaller in the multiscan case. Considering that silica glass may be the most important substrate compatible with the modern semiconductor industry, enhancing the writing efficiency of WGs in silica glass will be significant. Third, due to the relatively small refractive index change induced by fs lasers, reducing the bend loss is still a great challenge, and the effective working radius with reasonable performance is generally greater than 20 mm. More work is expected to decrease the bend loss for fabricating 3D complex photonic circuits with high density and purchasing the full fabrication capability of FLDW. Next, combining writing structures (e.g., WGs and nanogratings) with chemical etching and metal deposition will be an important step to construct photonic integrated devices, which also provides the possibility of realizing thermo-optic or electro-optical control over device functionality.[4,167,168] Furthermore, for the photonic integrated circuit devices, reducing the coupling loss between the WGs and other optical components, such as optical fibers, is also important, which can be achieved by modulating the refractive index and size of WGs. For example, temperature gradient-assisted fs laser writing offers a promising technique to tune the size of WGs and reduce the coupling loss significantly.[67] Packaging techniques for integrating various optical components and a large number of WGs are in demand.[169] In addition, WGs also provide a new platform for applications not yet achieved. For example, WGs are fascinating alternatives for programmable photonic circuits. Typically, the 3D designability gives WGs written by fs lasers superiority compared with the traditional 2D planar dielectric WGs.[4] Recently, integrated WGs with low power reconfigurability and reduced crosstalk have been produced by FLDW, and thermal phase shifting has been demonstrated, which indicates a very simple method for dynamic reconfiguration of the WGs.[168,170] These pave the way toward programmable photonic circuits, thus opening exciting perspectives in integrated photonics. WGs supporting orbital angular momentum modes possess an additional degree of freedom for modern optics and allow for the fabrication of a photonic chip for high-capacity communication and high-dimensional quantum information processing.[171,172] Integrated quantum memory may be also achievable by writing WGs in the rare-earth-ion-doped glass.[44]

In conclusion, this review reveals the rapidly growing photonic circuits written by fs lasers in glass. With important achievements and progress including improved technologies, such as beam shaping, multiscan, thermal annealing, predefect engineering, and composition engineering, the mechanisms and the recent photonic device applications, such as optical couplers, network devices, topological physics, quantum information processing, and astrophotonics, have been reviewed in detail. Future challenges and research directions have also been proposed. It is reasonable to expect further progress and additional applications of WGs and FLDW for the benefit of all-photonics networks in the future.

References

1. A. W. Elshaari et al., "Hybrid integrated quantum photonic circuits," *Nat. Photonics* **14**(5), 285–298 (2020).
2. M. Gräfe and A. Szameit, "Integrated photonic quantum walks," *J. Phys. B At. Mol. Opt. Phys.* **53**(7), 073001 (2020).
3. L. Li et al., "Integrated flexible chalcogenide glass photonic devices," *Nat. Photonics* **8**(8), 643–649 (2014).
4. W. Bogaerts et al., "Programmable photonic circuits," *Nature* **586**(7828), 207–216 (2020).

5. K. M. Davis et al., "Writing waveguides in glass with a femto-second laser," *Opt. Lett.* **21**(21), 1729–1731 (1996).

6. E. N. Glezer et al., "Three-dimensional optical storage inside transparent materials," *Opt. Lett.* **21**(24), 2023–2035 (1996).

7. D. Z. Wei et al., "Experimental demonstration of a three-dimensional lithium niobate nonlinear photonic crystal," *Nat. Photonics* **12**(10), 596–600 (2018).

8. Z. Wang, D. Z. Tan, and J. R. Qiu, "Single-shot photon recording for three-dimensional memory with prospects of high capacity," *Opt. Lett.* **45**(22), 6274–6277 (2020).

9. K. J. Sugioka and Y. Cheng, "Ultrafast lasers—reliable tools for advanced materials processing," *Light Sci. Appl.* **3**(4), e149 (2014).

10. W. J. Yang, P. G. Kazansky, and Y. P. Svirko, "Non-reciprocal ultrafast laser writing," *Nat. Photonics* **2**(2), 99–104 (2008).

11. D. Z. Tan et al., "Single-pulse-induced ultra-fast spatial cluster-ing of metal in glass: fine tunability and application," *Adv. Photonics Res.* (2000121) (2021).

12. Y. Hu et al., "Chiral assemblies of laser-printed micropillars directed by asymmetrical capillary force," *Adv. Mater.* **32**(31), 2002356 (2020).

13. S. Jiang et al., "Multifunctional Janus microplates arrays actuated by magnetic fields for water/light switches and bio-inspired assimilatory coloration," *Adv. Mater.* **31**(15), 1807507 (2019).

14. T. Meany et al., "Laser written circuits for quantum photonics," *Laser Photonics Rev.* **9**(4), 363–384 (2015).

15. D. Z. Tan et al., "Femtosecond laser induced phenomena in trans-parent solid materials: fundamentals and applications," *Prog. Mater. Sci.* **76**, 154–228 (2016).

16. K. Miura et al., "Photowritten optical waveguides in various glasses with ultrashort pulse laser," *Appl. Phys. Lett.* **71**(23), 3329–3331 (1997).

17. S. M. Eaton, H. Zhang, and P. R. Herman, "Heat accumulation effects in femtosecond laser written waveguides with variable repetition rate," *Opt. Express* **13**(12), 4708–4716 (2005).

18. A. Szameit and S. Nolte, "Discrete optics in femtosecond-laser written photonic structures," *J. Phys. B At. Mol. Opt. Phys.* **43**(16), 163001 (2010).

19. R. G. H. van Uden et al., "Ultra-high-density spatial division multiplexing with a few-mode multicore fibre," *Nat. Photonics* **8**(11), 865–870 (2014).

20. X. Y. Xu et al., "Shining light on quantum transport in fractal networks," arXiv:2005.13385v1 (2020).

21. A. Couairona and A. Mysyrowicz, "Femtosecond filamentation in transparent media," *Phys. Rep.* **441**(2-4), 47–189 (2007).

22. Q. Sun et al., "Effect of spherical aberration on the propagation of a tightly focused femtosecond laser pulse inside fused silica," *J. Opt. A Pure Appl. Opt.* **7**(11), 655–659 (2005).

23. Y. Cheng et al., "Control of the cross-sectional shape of a hollow microchannel embedded in photostructurable glass by use of a femtosecond laser," *Opt. Lett.* **28**(1), 55–57 (2003).

24. N. Bisch et al., "Adaptive optics aberration correction for deep direct laser written waveguides in the heating regime," *Appl. Phys. A* **125**(5), 364 (2019).

25. M. Ams et al., "Slit beam shaping method for femtosecond laser direct-write fabrication of symmetric waveguides in bulk glasses," *Opt. Express* **13**(15), 5676–5681 (2005).

26. V. D. Blanco et al., "Deep subsurface waveguides with circular cross section produced by femtosecond laser writing," *Appl. Phys. Lett.* **91**(5), 051104 (2007).

27. D. Liu et al., "Influence of focusing depth on the microfabrica-tion of waveguides inside silica glass by femtosecond laser direct writing," *Appl. Phys. A* **84**(3), 257–260 (2006).

28. S. Gross and M. J. Withford, "Ultrafast-laser-inscribed 3D inte-grated photonics: challenges and emerging applications," *Nanophotonics* **4**(3), 332–335 (2015).

29. G. Cerullo et al., "Femtosecond micromachining of symmetric waveguides at 1.5 μm by astigmatic beam focusing," *Opt. Lett.* **27**(21), 1938–1940 (2002).

30. F. He et al., "Fabrication of microfluidic channels with a circular cross section using spatiotemporally focused femtosecond laser pulses," *Opt. Lett.* **35**(7), 1106–1108 (2010).

31. R. Osellame et al., "Femtosecond writing of active optical wave-guides with astigmatically shaped beams," *J. Opt. Soc. Am. B* **20**(7), 1559–1567 (2003).

32. P. R. Varona et al., "Slit beam shaping technique for femtosecond laser inscription of enhanced plane-by-plane FBGs," *J. Lightwave Technol.* **38**(16), 4526–4532 (2020).

33. V. D. Michele et al., "Near-IR- and UV-femtosecond laser wave-guide inscription in silica glasses," *Opt. Mater. Express* **9**(12), 4624–4633 (2019).

34. M. Royon et al., "X-ray preconditioning for enhancing refractive index contrast in femtosecond laser photoinscription of em-bedded waveguides in pure silica," *Opt. Mater. Express* **9**(1), 65–74 (2019).

35. K. Mishchik et al., "Photoinscription domains for ultrafast laser writing of refractive index changes in BK7 borosilicate crown optical glass," *Opt. Mater. Express* **3**(1), 67–85 (2013).

36. G. D. Marshall et al., "Directly written monolithic waveguide laser incorporating a distributed feedback waveguide-Bragg grating," *Opt. Lett.* **33**(9), 956–958 (2008).

37. D. Marshall, M. Ams, and M. J. Withford, "Direct laser written waveguide–Bragg gratings in bulk fused silica Graham," *Opt. Lett.* **31**(18), 2690–2692 (2006).

38. A. R. De la Cruz et al., "Modeling of astigmatic-elliptical beam shaping during fs-laser waveguide writing including beam trun-cation and diffraction effects," *Appl. Phys. A* **104**(2), 687–693 (2011).

39. Y. Wang et al., "Quantum topological boundary states in quasi-crystals," *Adv. Mater.* **31**(49), 1905624 (2019).

40. R. J. Ren et al., "Identical quantum sources integrated on a single silica chip," arXiv:2005.12918 (2020).

41. J. P. Brub and R. Valle, "Femtosecond laser direct inscription of surface skimming waveguides in bulk glass," *Opt. Lett.* **41**(13), 3074–3077 (2016).

42. J. P. Bérubé et al., "Femtosecond laser direct inscription of mid-IR transmitting waveguides in BGG glasses," *Opt. Mater. Express* **7**(9), 3124–3135 (2017).

43. C. Y. Wang, J. Gao, and X. M. Jin, "On-chip rotated polarization directional coupler fabricated by femtosecond laser direct writ-ing," *Opt. Lett.* **44**(1), 102–105 (2019).

44. C. Liu et al., "On-demand quantum storage of photonic qubits in an on-chip waveguide," *Phys. Rev. Lett.* **125**(26), 260504 (2020).

45. R. Osellame et al., "Lasing in femtosecond laser written optical waveguides," *Appl. Phys. A* **93**(1), 17–26 (2008).

46. Z. H. Wang et al., "Interferometric characterization of pulse front tilt of spatiotemporally focused femtosecond laser pulses," *Opt. Express* **22**(21), 26328–26337 (2014).

47. B. Sun et al., "Four-dimensional light shaping: manipulating ul-trafast spatiotemporal foci in space and time," *Light Sci. Appl.* **7**(1), 17117 (2018).

48. A. Patel et al., "Non-paraxial polarization spatio-temporal cou-pling in ultrafast laser material processing," *Laser Photonics Rev.* **11**(3), 1600290 (2017).

49. R. Kammel et al., "Simultaneous spatial and temporal focusing: a route towards confined nonlinear materials processing," *Proc. SPIE* **9736**, 97360T (2016).

50. P. Wang et al., "Aberration-insensitive three-dimensional micro-machining in glass with spatiotemporally shaped femtosecond laser pulses," *Opt. Lett.* **43**(15), 3485–3488 (2018).

51. F. He et al., "Independent control of aspect ratios in the axial and lateral cross sections of a focal spot for three-dimensional femto-second laser micromachining," *New J. Phys.* **13**(8), 083014 (2011).

52. E. Block et al., "Integrated single grating compressor for variable pulse front tilt in simultaneously spatially and temporally focused systems," *Opt. Lett.* **39**(24), 6915–6918 (2014).

53. J. Squier et al., "High average power Yb:CaF femtosecond amplifier with integrated simultaneous spatial and temporal focusing for laser material processing," *Appl. Phys. A* **114**(1), 209–214 (2014).

54. D. N. Vitek et al., "Temporally focused femtosecond laser pulses for low numerical aperture micromachining through optically transparent materials," *Opt. Express* **18**(17), 18086–18094 (2010).

55. G. Zhu et al., "Simultaneous spatial and temporal focusing of femtosecond pulses," *Opt. Express* **13**(6), 2153–2159 (2005).

56. B. Leshem et al., "When can temporally focused excitation be axially shifted by dispersion?" *Opt. Express* **22**(6), 7087–7098 (2014).

57. R. Kammel et al., "Enhancing precision in fs-laser material processing by simultaneous spatial and temporal focusing," *Light Sci. Appl.* **3**(5), e169 (2014).

58. P. S. Salter et al., "Adaptive slit beam shaping for direct laser written waveguides," *Opt. Lett.* **37**(4), 470–472 (2012).

59. L. Huang et al., "Aberration correction for direct laser written waveguides in a transverse geometry," *Opt. Express* **24**(10), 10565–10574 (2016).

60. P. S. Salter et al., "Adaptive optics in laser processing," *Light Sci. Appl.* **8**(1), 110 (2019).

61. M. Sakakura et al., "Fabrication of three-dimensional 1 × 4 splitter waveguides inside a glass substrate with spatially phase modulated laser beam," *Opt. Express* **18**(12), 12136–12143 (2010).

62. M. Pospiech et al., "Single-sweep laser writing of 3D-waveguide devices," *Opt. Express* **18**(7), 6994–7001 (2010).

63. C. Mauclair et al., "Dynamic ultrafast laser spatial tailoring for parallel micromachining of photonic devices in transparent materials," *Opt. Express* **17**(5), 3531–3542 (2009).

64. P. S. Salter and M. J. Booth, "Dynamic optical methods for direct laser written waveguides," *Proc. SPIE* **8613**, 86130A (2013).

65. Y. Nasu, M. Kohtoku, and Y. Hibino, "Low-loss waveguides written with a femtosecond laser for flexible interconnection in a planar light-wave circuit," *Opt. Lett.* **30**(7), 723–725 (2005).

66. R. Keil et al., "Hybrid waveguide-bulk multi-path interferometer with switchable amplitude and phase," *APL Photonics* **1**(8), 081302 (2016).

67. D. Z. Tan et al., "Fabricating low loss waveguides over a large depth in glass by temperature gradient assisted femtosecond laser writing," *Opt. Lett.* **45**(14), 3941–3944 (2020).

68. S. Gross et al., "Three-dimensional ultra-broadband integrated tapered mode multiplexers," *Laser Photonics Rev.* **8**(5), L81–L85 (2014).

69. R. Mary, D. Choudhury, and A. K. Kar, "Applications of fiber lasers for the development of compact photonic devices," *IEEE J. Sel. Top. Quantum. Electron* **20**(5), 72–84 (2014).

70. M. D. Mackenzie et al., "GLS and GLSSe ultrafast laser inscribed waveguides for mid-IR supercontinuum generation," *Opt. Mater. Express* **9**(2), 643–651 (2019).

71. Z. M. Liu et al., "Suppression of bend loss in writing of three-dimensional optical waveguides with femtosecond laser pulses," *Sci. China-Phys. Mech. Astron.* **61**(7), 070322 (2018).

72. R. Heilmann et al., "Tapering of femtosecond laser-written waveguides," *Appl. Opt.* **57**(3), 377–381 (2018).

73. N. D. Psaila et al., "Femtosecond laser inscription of optical waveguides in Bismuth ion doped glass," *Opt. Express* **14**(22), 10452–10459 (2006).

74. H. L. Butcher et al., "Ultrafast laser-inscribed mid-infrared evanescent field directional couplers in GeAsSe chalcogenide glass," *OSA Continuum.* **1**(1), 221–228 (2018).

75. L. Helen et al., "Demonstration and characterization of ultrafast laser-inscribed mid-infrared waveguides in chalcogenide glass IG2," *Opt. Express* **26**(8), 10930–10943 (2018).

76. G. Demetriou et al., "Nonlinear refractive index of ultrafast laser inscribed waveguides in gallium lanthanum sulphide," *Appl. Opt.* **56**(19), 5407–5411 (2017).

77. R. R. Thomson, A. K. Kar, and J. Allington-Smith, "Ultrafast laser inscription: an enabling technology for astrophotonics," *Opt. Express* **17**(3), 1963–1969 (2009).

78. R. R. Thomson et al., "Ultrafast laser inscription of an integrated photonic lantern," *Opt. Express* **19**(6), 5698–5705 (2011).

79. G. Douglass et al., "Femtosecond laser written arrayed waveguide gratings with integrated photonic lanterns," *Opt. Express* **26**(2), 1497–1505 (2018).

80. B. R. M. Norris et al., "First on-sky demonstration of an integrated-photonic nulling interferometer: the GLINT instrument," *Mon. Not. R. Astron. Soc.* **491**(3), 4180–4193 (2020).

81. L. A. Fernandes et al., "Stress induced birefringence tuning in femtosecond laser fabricated waveguides in fused silica," *Opt. Express* **20**(22), 24103–24114 (2012).

82. G. Corrielli et al., "Symmetric polarization-insensitive directional couplers fabricated by femtosecond laser writing," *Opt. Express* **26**(12), 15101–15109 (2018).

83. Z. M. Liu et al., "Fabrication of an optical waveguide-mode-field compressor in glass using a femtosecond laser," *Materials* **11**(10), 1926 (2018).

84. M. Sakakura et al., "Thermal and shock induced modification inside a silica glass by focused femtosecond laser pulse," *J. Appl. Phys.* **109**(2), 023503 (2011).

85. V. R. Bhardwaj et al., "Stress in femtosecond-laser-written waveguides in fused silica," *Opt. Lett.* **29**(12), 1312–1314 (2004).

86. A. Arriola et al., "Low bend loss waveguides enable compact, efficient 3D photonic chips," *Opt. Express* **21**(3), 2978–2986 (2013).

87. O. S. Narayanaswamy, "Annealing of glass," *Glass Sci. Technol.* **3**, 275–318 (1986).

88. H. E. Hagy, "Fine annealing of optical glass for low residual stress and refractive index homogeneity," *Appl. Opt.* **7**(5), 833–835 (1968).

89. N. Ollier et al., "Relaxation study of pre-densified silica glasses under 2.5 MeV electron irradiation," *Sci. Rep.* **9**(1), 1227 (2019).

90. J. J. Witcher et al., "Thermal annealing of femtosecond laser written structures in silica glass," *Opt. Mater. Express* **3**(4), 502–510 (2013).

91. B. H. Babu et al., "Systematic control of optical features in aluminosilicate glass waveguides using direct femtosecond laser writing," *Opt. Mater.* **72**, 501–507 (2017).

92. P. Dekker et al., "Annealing dynamics of waveguide Bragg gratings: evidence of femtosecond laser induced colour centres," *Opt. Express* **18**(4), 3274–3283 (2010).

93. J. D. Musgraves, K. Richardson, and H. Jain, "Laser-induced structural modification, its mechanisms, and applications in glassy optical materials," *Opt. Mater. Express* **1**(5), 921–935 (2011).

94. X. W. Wang et al., "Analysis of defects patterned by femtosecond pulses inside KBr and SiO_2 glass," *Appl. Phys. A* **122**(3), 194 (2016).

95. T. T. Fernandez et al., "Ion migration assisted inscription of high refractive index contrast waveguides by femtosecond laser pulses in phosphate glass," *Opt. Lett.* **38**(24), 5248–5251 (2013).

96. T. T. Fernandez et al., "Revisiting ultrafast laser inscribed waveguide formation in commercial alkali-free borosilicate glasses," *Opt. Express* **28**(7), 10153–10164 (2020).

97. P. Moreno-Zarate et al., "Role of the La/K compositional ratio in the properties of waveguides written by fs-laser induced element redistribution in phosphate-based glasses," *Materials* **13**(6), 1275 (2020).

98. T. T. Fernandez et al., "Bespoke photonic devices using ultrafast laser driven ion migration in glasses," *Prog. Mater. Sci.* **94**, 68–113 (2018).

99. M. Macias-Montero et al., "Waveguide tapers fabrication by femtosecond laser induced element redistribution in glass," *J. Lightwave Technol.* **38**(23), 6578–6583 (2020).

100. L. Bressel et al., "Femtosecond laser induced density changes in GeO$_2$ and SiO$_2$ glasses: fictive temperature effect," *Opt. Mater. Express* **1**(4), 605–613 (2011).

101. J. M. Oliveira et al., "Waveguides written in silver-doped tellurite glasses," *Opt. Mater.* **101**, 109767 (2020).

102. N. Riesen et al., "Femtosecond direct-written integrated mode couplers," *Opt. Express* **22**(24), 29855–29861 (2014).

103. Y. Duan et al., "Time dependent study of femtosecond laser written waveguide lasers in Yb-doped silicate and phosphate glass," *Opt. Mater. Express* **5**(2), 416–422 (2015).

104. K. Minoshima et al., "Fabrication of coupled mode photonic devices in glass by nonlinear femtosecond laser materials processing," *Opt. Express* **10**(15), 645–652 (2002).

105. K. Suzuki et al., "Characterization of symmetric [3 × 3] directional couplers fabricated by direct writing with a femtosecond laser oscillator," *Opt. Express* **14**(6), 2335–2343 (2006).

106. S. Gross et al., "Ultrafast laser-written sub-components for space division multiplexing," in *Opt. Fiber Commun. Conf.*, OSA, p. W1A.1 (2020).

107. J. Lapointe et al., "Making smart phones smarter with photonics," *Opt. Express* **22**(13), 15473–15483 (2014).

108. R. Heilmann et al., "Arbitrary photonic wave plate operations on chip: realizing Hadamard, Pauli-X and rotation gates for polarisation qubits," *Sci. Rep.* **4**(1), 4118 (2015).

109. L. A. Fernandes et al., "Femtosecond laser fabrication of birefringent directional couplers as polarisation beam splitters in fused silica," *Opt. Express* **19**(13), 11992–11999 (2011).

110. W. J. Yang et al., "Low loss photonic components in high index bismuth borate glass by femtosecond laser direct writing," *Opt. Express* **16**(20), 16215–16226 (2008).

111. I. Pitsios et al., "Geometrically controlled polarisation processing in femtosecond-laser-written photonic circuits," *Sci. Rep.* **7**(1), 11342 (2017).

112. G. Corrielli et al., "Rotated waveplates in integrated waveguide optics," *Nat. Commun.* **5**(1), 4249 (2014).

113. L. Sansoni et al., "Polarization entangled state measurement on a chip," *Phys. Rev. Lett.* **105**(20), 200503 (2010).

114. R. S. Luís et al., "1.2 Pb/s throughput transmission using a 160 μm cladding, 4-core, 3-mode fiber," *J. Lightwave Technol.* **37**(8), 1798–1804 (2019).

115. V. A. Amorim et al., "Monolithic add–drop multiplexers in fused silica fabricated by femtosecond laser direct writing," *J. Lightwave Technol.* **35**(17), 3615–3621 (2017).

116. I. V. Dyakonov et al., "Laser-written polarizing directional coupler with reduced interaction length," *Opt. Lett.* **42**(20), 4231–4234 (2017).

117. T. Mizuno et al., "Dense space-division multiplexed transmission systems using multi-core and multi-mode fiber," *J. Lightwave Technol.* **34**(2), 582–592 (2016).

118. N. Riesen et al., "Monolithic mode-selective few-mode multicore fiber multiplexers," *Sci. Rep.* **7**(1), 6971 (2017).

119. B. Guan et al., "Free-space coherent optical communication with orbital angular, momentum multiplexing/demultiplexing using a hybrid 3D photonic integrated circuit," *Opt. Express* **22**(1), 145–156 (2014).

120. G. Djogo et al., "Femtosecond laser additive and subtractive micro-processing: enabling a high-channel-density silica interposer for multicore fibre to silicon-photonic packaging," *Int. J. Extreme. Manuf.* **1**(4), 045002 (2019).

121. R. R. Thomson et al., "Ultrafast-laser inscription of a three dimensional fan-out device for multicore fiber coupling applications," *Opt. Express* **15**(18), 11691–11697 (2007).

122. M. Mirshafiei et al., "Glass interposer for short reach optical connectivity," *Opt. Express* **24**(11), 12375–12384 (2016).

123. C. Mikael et al., "Photonic Floquet topological insulators," *Nature* **496**(7444), 196–200 (2013).

124. N. Spagnolo, "Experimental validation of photonic boson sampling," *Nat. Photonics* **8**(8), 615–620 (2014).

125. L. Lu, J. D. Joannopoulos, and M. Soljačić, "Topological photonics," *Nat. Photonics* **8**(11), 821–829 (2014).

126. M. Kim, Z. Jacob, and J. Rho, "Recent advances in 2D, 3D and higher-order topological photonics," *Light Sci. Appl.* **9**(1), 130 (2020).

127. M. C. Rechtsman et al., "Photonic Floquet topological insulators," *Nature* **496**(7444), 196–200 (2013).

128. M. Kremer et al., "A square-root topological insulator with non-quantized indices realized with photonic Aharonov-Bohm cages," *Nat. Commun.* **11**(1), 907 (2020).

129. L. J. Maczewsky et al., "Fermionic time-reversal symmetry in a photonic topological insulator," *Nat. Mater.* **19**(8), 855–860 (2020).

130. S. Weimann et al., "Topologically protected bound states in photonic parity–time-symmetric crystals," *Nat. Mater.* **16**(4), 433–438 (2017).

131. G. G. Pyrialakos et al., "Symmetry-controlled edge states in the type-II phase of Dirac photonic lattices," *Nat. Commun.* **11**(1), 2074 (2020).

132. J. Noh et al., "Observation of photonic topological valley Hall edge states," *Phys. Rev. Lett.* **120**(6), 063902 (2018).

133. Z. J. Yang et al., "Photonic Floquet topological insulators in a fractal lattice," *Light Sci. Appl.* **9**(1), 128 (2020).

134. S. Mukherjee and M. C. Rechtsman, "Observation of Floquet solitons in a topological bandgap," *Science* **368**(6493), 856–859 (2020).

135. O. Zilberberg et al., "Photonic topological boundary pumping as a probe of 4D quantum Hall physics," *Nature* **553**(7686), 59–62 (2018).

136. J. Noh et al., "Topological protection of photonic mid-gap defect modes," *Nat. Photonics* **12**(7), 408–415 (2018).

137. S. Stützer et al., "Photonic topological Anderson insulators," *Nature* **560**(7719), 461–465 (2018).

138. E. Lustig et al., "Photonic topological insulator in synthetic dimensions," *Nature*, **567**(7748), 356–360 (2019).

139. Y. Lumer et al., "Light guiding by artificial gauge fields," *Nat. Photonics* **13**(5), 339–345 (2019).

140. A. E. Hassan et al., "Corner states of light in photonic waveguides," *Nat. Photonics* **13**(10), 697–700 (2019).

141. Y. Wang et al., "Quantum topological boundary states in quasicrystals," *Adv. Mater.* **31**(49), 1905624 (2019).

142. J. W. Wang et al., "Integrated photonic quantum technologies," *Nat. Photonics* **14**(5), 273–284 (2020).

143. D. J. Brod et al., "Photonic implementation of boson sampling: a review," *Adv. Photonics* **1**(3), 034001 (2019).

144. N. Spagnolo et al., "Three-photon bosonic coalescence in an integrated tritter," *Nat. Commun.* **4**(1), 1606 (2013).

145. T. Giordani et al., "Experimental statistical signature of many-body quantum interference," *Nat. Photonics* **12**(3), 173–178 (2018).

146. A. Crespi et al., "Anderson localization of entangled photons in an integrated quantum walk," *Nat. Photonics* **7**(4), 322–328 (2013).

147. J. L. Tambasco et al., "Quantum interference of topological states of light," *Sci. Adv.* **4**(9), eaat3187 (2018).

148. C. Antón et al., "Interfacing scalable photonic platforms: solid-state based multi-photon interference in a reconfigurable glass chip," *Optica* **6**(12), 1471–1477 (2019).

149. H. Tang et al., "Experimental quantum fast hitting on hexagonal graphs," *Nat. Photonics* **12**(12), 754–758 (2018).

150. X. Y. Xu et al., "A scalable photonic computer solving the subset sum problem," *Sci. Adv.* **6**(5), eaay5853 (2020).

151. H. Tang et al., "Experimental two-dimensional quantum walk on a photonic chip," *Sci. Adv.* **4**(5), eaat3174 (2018).

152. Z. Y. Shi et al., "Quantum fast hitting on glued trees mapped on a photonic chip," *Optica* **7**(6), 613–618 (2020).

153. Y. Wang et al., "Topologically protected quantum entanglement," arXiv:1903.03015v1 (2019).

154. J. Noh et al., "Experimental observation of optical Weyl points and Fermi arc-like surface states," *Nat. Phys.* **13**(6), 611–617 (2017).

155. A. Cerjan et al., "Experimental realization of a Weyl exceptional ring," *Nat. Photonics* **13**(9), 623–628 (2019).

156. A. Crespi et al., "Suppression law of quantum states in a 3D photonic fast Fourier transform chip," *Nat. Commun.* **7**(1), 10469 (2016).

157. A. Saviauk et al., "3D-integrated optics component for astronomical spectro-interferometry," *Appl. Opt.* **52**(19), 4556–4565 (2013).

158. D. G. MacLachlan et al., "Development of integrated mode reformatting components for diffraction-limited spectroscopy," *Opt. Lett.* **41**(1), 76–79 (2016).

159. R. J. Harris et al., "Photonic spatial reformatting of stellar light for diffraction-limited spectroscopy," *Mon. Not. R. Astron. Soc.* **450**(1), 428–434 (2015).

160. N. Cvetojevic et al., "Modal noise in an integrated photonic lantern fed diffraction-limited spectrograph," *Opt. Express* **25**(21), 25546–25565 (2017).

161. R. Diener et al., "Towards 3D-photonic, multi-telescope beam combiners for midinfrared astrointerferometry," *Opt. Express* **25**(16), 19262–19274 (2017).

162. T. Gretzinger et al., "Towards a photonic mid-infrared nulling interferometer in chalcogenide glass," *Opt. Express* **27**(6), 8626–8638 (2019).

163. J. Tepper et al., "Ultrafast laser inscription in ZBLAN integrated optics chips for mid-IR beam combination in astronomical interferometry," *Opt. Express* **25**(17), 20642–20653 (2017).

164. A. Arriola et al., "Mid-infrared astrophotonics: study of ultrafast laser induced index change in compatible materials," *Opt. Mater. Express* **7**(3), 698–711 (2017).

165. N. Jovanovic et al., "Integrated photonic building blocks for next-generation astronomical instrumentation I: the multimode waveguide," *Opt. Express* **20**(15), 17029–17043 (2012).

166. J. Tepper et al., "Integrated optics prototype beam combiner for long baseline interferometry in the L and M bands," *Astron. Astrophys.* **602**, A66 (2017).

167. N. Psaila, "3D laser direct writing for advanced photonic integration," *Proc. SPIE* **10924**, 109240U (2019).

168. F. Ceccarelli et al., "Low power reconfigurability and reduced crosstalk in integrated photonic circuits fabricated by femtosecond laser micromachining," *Laser Photonics Rev.* **14**(10), 2000024 (2020).

169. E. Perez et al., "Automated on-axis direct laser writing of coupling elements for photonic chips," *Opt. Express* **28**(26), 39340–39353 (2020).

170. F. Ceccarelli et al., "Thermal phase shifters for femtosecond laser written photonic integrated circuits," *J. Lightwave Technol.* **37**(17), 4275–4281 (2019).

171. Y. Chen et al., "Mapping twisted light into and out of a photonic chip," *Phys. Rev. Lett.* **121**(23), 233602 (2018)

172. Y. Chen et al., "Vector vortex beam emitter embedded in a photonic chip," *Phys. Rev. Lett.* **124**(15), 153601 (2020).

Dezhi Tan is an associate professor in the College of Optical Science and Engineering at Zhejiang University, China. He received his BS and PhD degrees in materials science and engineering from Zhejiang University in 2009 and 2014, respectively. He worked as a postdoc at Polytechnique Montreal (Canada), the JSPS fellow in Kyoto University (Japan), and a research professor in the Institute for Basic Science (Korea). His current research interest is focused on the study of ultrafast laser–matter interaction and the fabrication of micro/nanostructures and devices in transparent media.

Jianrong Qiu is a professor in the College of Optical Science and Engineering at Zhejiang University, China. He specializes in laser–matter interaction and optical materials. He is the chair professor of the Cheung Kong Scholars Program, and a fellow of the Optical Society of America (OSA), the American Ceramic Society (ACS), the International Glass Commission, and the Chinese Ceramics Society. He is also the vice chairman of Photoelectronic Glasses Branch and an associate editor (or international advisory board member) of *Asian J. Ceram Soc., Int. J. Appl. Glass Sci.*, and *J. Non-Cryst. Solids*.

Biographies of the other authors are not available.